# Mathematical Modeling on the Growth and Removal of Non-metallic Inclusions in the Molten Steel in a Two-Strand Continuous Casting Tundish

HAITAO LING, LIFENG ZHANG, and HONG LI

In the current study, mathematical models were developed to predict the transient concentration and size distribution of inclusions in a two-strand continuous casting tundish. The collision and growth of inclusions were considered. The contribution of turbulent collision and Stokes collision was evaluated. The removal of inclusions from the top surface was modeled by considering the properties of inclusions and the molten steel, such as the wettability, density, size, and interfacial tension. The effect of composition of inclusions on the collision of inclusions was included through the Hamaker constant. Meanwhile, the effect of the turbulent fluctuation velocity on the removal of inclusions at the top surface was also studied. Inclusions in steel samples were detected using automatic SEM Scanning so that the amount, morphology, size, and composition of inclusions were achieved. In the simulation, the size distribution of inclusions at the end steel refining was used as the initial size distribution of inclusions at tundish inlet. The equilibrium time when the collision and coalescence of inclusions reached the steady state was equal to 3.9 times of the mean residence time. When Stokes collision, turbulent collision, and removal by floating were included, the removal fraction of inclusions was 16.4 pct. Finally, the removal of solid and liquid inclusions, such as $Al_2O_3$, $SiO_2$, and $12CaO \cdot 7Al_2O_3$, at the interface between the molten steel and slag was studied. Compared with $12CaO \cdot 7Al_2O_3$ inclusions, the silica and alumina inclusions were much easier to be removed from the molten steel and their removal fractions were 36.5 and 39.2 pct, respectively.

## I. INTRODUCTION

CONTINUOUS casting tundish serves as a buffer and acts as distributors of the molten steel between the ladle and the mold. It shows various metallurgical functions, such as optimization of molten steel flow, inclusions separation, alloy trimming of steel, superheat control, and thermal homogenization. Nowadays, to realize an optimal flow and better cleanliness of the liquid steel, the design of the tundish needs to meet the targets of (1) high average residence time; (2) small dead volumes and non-short circuit flow; (3) large volume of laminar flow region; (4) forced collision of inclusions in suitable turbulent zones and floating of inclusions at other zones, assimilated by the cover slag; and (5) avoiding the excessive top surface level fluctuation and reoxidation by air absorption.

Flow control devices, such as weirs, dams, turbulence inhibitors, and baffles, have been installed at suitable positions in the tundish, with a purpose to improve the flow pattern of the molten steel and promote the removal of inclusions. A large number of inclusions, especially coagulated large-sized ones, have a detrimental effect on the quality of steel products. Steel cleanliness depends greatly on the amount, the size distribution, morphology, and composition of non-metallic inclusions in the steel. They should be under strict control during the production of high clean steels. An extensive review in the evaluation and control of steel cleanliness has been made by the current author, Zhang and Thomas, in 2003.[1] According to the steel grade and its end use, the requirements of steel cleanliness are different. For instance, the total oxygen and maximum size of inclusions for ball bearings are needed to be less than 10 ppm and 15 $\mu$m, respectively,[2–4] and they are required to be less than 15 ppm and 10 $\mu$m for tire cord steels.[2] Many defects in the steel products caused by inclusions are mentioned in the literature. Lange[5] found that the cracked flanges were caused by sulfide and oxide inclusions in the low carbon Al-killed steel. Park and Todoroki[6] reported that swollen defects on a deeply draw product were induced by $MgO \cdot Al_2O_3$ spinel inclusions. Van Ende et al.[7] found that the submerged entry nozzle was seriously clogged due to the accumulation of $Al_2O_3$ inclusions generated by reoxidation using the population density

HAITAO LING, Ph.D. Student, and LIFENG ZHANG, Professor, are with the Beijing Key Laboratory of Green Recycling and Extraction of Metals (GREM), University of Science and Technology Beijing (USTB), Beijing 100083, China, and also with the School of Metallurgical and Ecological Engineering, University of Science and Technology Beijing (USTB). Contact e-mail: zhanglifeng@ustb.edu.cn HONG LI, Professor, is with the School of Metallurgical and Ecological Engineering of University of Science and Technology Beijing (USTB).

function (PDF) analysis. In addition, inclusions in steel can be categorized to exogenous inclusions and endogenous inclusions. For instance, when adding the deoxidizer, the deoxidization element reacts quickly with the dissolved oxygen. The ladle slag or the tundish slag is often entrained into the molten steel from the ladle shroud. Besides, the collision and coalescence of inclusions always occur and the amount of large-sized inclusions gradually increases. Due to the buoyancy force and bubble attachment, inclusions float up and are adsorbed by the cover slag. Figure 1 shows the sources and removal of inclusions in the molten steel.

There have been many reported studies on the collision and coalescence of particles in liquids, especially for molten steel system (Table I). As early as 1956, Saffman and Turner[8] established a population balance equation and developed a turbulent collision model to calculate the generation and dissipation of small drops in a turbulent fluid. Nakanishi and Szekely[9] analyzed the rate of Al-deoxidation of the molten steel in an ASEA–SKF furnace using Saffman and Turner's theory and assuming that inclusions with radius larger than 16 $\mu$m disappeared instantly. Higashitani and Yamaguchi[10] introduced a coagulation coefficient $\alpha$ to the Saffman–Turner model, taking into account the effect of the viscous force and van der Waals force. Tozawa and Kato[11] considered the effect of the fractal dimension on the coalescence of cluster-shaped alumina inclusions in a 70 t tundish. Their calculated results showed a good agreement with the results measured in the actual machine. Nakaoka and Taniguchi[12] established a particle size grouping (PSG) method with an accurate mass balance of particles and studied the agglomeration of polyvinyl-toluene latex particles in a NaCl aqueous solution. They found that the agglomeration curves for various particle concentrations and agitation speeds agreed well with the calculated results by the PSG method. Zhang[13–17] studied the nucleation and growth of alumina inclusions during steel deoxidation using numerical simulation. In their study, the main control factors included Ostwald-ripening, Brownian collision, Stokes collision, and turbulent collision. The time evolution of the size distribution of inclusions from nm to hundred-$\mu$m has been successfully predicted. Recently, Xu and Thomas[18] proposed an efficient PSG population-balance method to calculate the diffusion-controlled nucleation and growth of precipitates in microalloyed steels. They found that the computed fraction of aluminum nitride precipitated and the mean size, volume fraction, size distribution of niobium carbide showed encouraging agreement with previous experimental measurements. Since 2000, many investigators paid more attention to the collision, growth and removal of inclusions during ladle refining process.[19–25] The argon bubble injecting operations improved the removal efficiency of inclusions.[26,27] However, the effect of composition of inclusions on the collision of inclusions is seldom considered.

In previous investigations, the removal of inclusions at the top surface in metallurgical vessels, such as ladle, tundish, mold, *etc.*, was modeled by defining a removal flux at the boundary condition[11,14,19,28,29] or adding a removal source in the transport equation.[20,22–25,30–32] Furthermore, the Hamaker constant was a given value of $2.3 \times 10^{-20}$ or $0.45 \times 10^{-20}$ J for collision and coalescence of inclusions.[11,19,22] If the density and size of inclusions are known, the removal flux or source will be determined. But in some cases, the behavior of inclusions at the interface between the liquid steel and the slag involves the separation from the molten steel and re-entrainment back into the bulk. Meanwhile, the Hamaker constant depends on the composition of inclusions and its value is different for different types of inclusions. In the current study, a new removal condition was proposed to simulate the removal of inclusion at the top surface in the tundish, based on the properties of inclusions and the liquid steel, such as wettability, density, size, and interfacial tension. Besides, the effect of the turbulent fluctuation velocity and the Hamaker constant on the collision and coalescence of inclusions was also included. Finally, the removal of solid and liquid inclusions from the top slag, such as $Al_2O_3$, $SiO_2$ and $12CaO\cdot7Al_2O_3$, was simulated and discussed.

## II. MATHEMATICAL FORMULATION

The tundish was two-strand and with a capacity of 35 t. The weir with a hole and the impact pad were used to control the flow of molten steel in the tundish. The shape of the hole was truncated cone and horizontal through the weir. The impact pad was installed at the bottom of the pouring zone and with a $500 \times 500$ mm$^2$ cross section area. The casting speed was 1.0 m/minute resulting in a 40-minute casting time per heat and the depth of molten steel in the tundish was 925 mm under the steady state. The dimensions of the tundish and parameters of molten steel are shown in Figure 2 and Table II.

In the current simulations, the collision and removal of inclusions were coupled with the flow of the liquid steel in the tundish. The size distribution of inclusions was defined by particle size grouping method. The following assumptions were included in the study. The molten steel in the tundish was assumed to be an incompressible Newtonian fluid. Inclusions were spherical and the effect of the fractal dimension on the morphology of inclusions was negligible. However, the density of inclusions considered the effect of composition. The mechanical erosion of the lining refractory and re-entrainment of the molten slag in the tundish were ignored.

### A. *Fluid Flow and Residence Time*

The continuity equation, Reynolds-averaged Navier–Stokes equations, standard $k - \varepsilon$ equations, and energy transport equation were solved to obtain the flow field and temperature distribution in the tundish. The effect of natural convection on the fluid flow was considered by incorporating the Boussinesque's term ($\beta(T_0 - T)\rho g_i$) into the vertical direction of the momentum balance equation.[33,34]
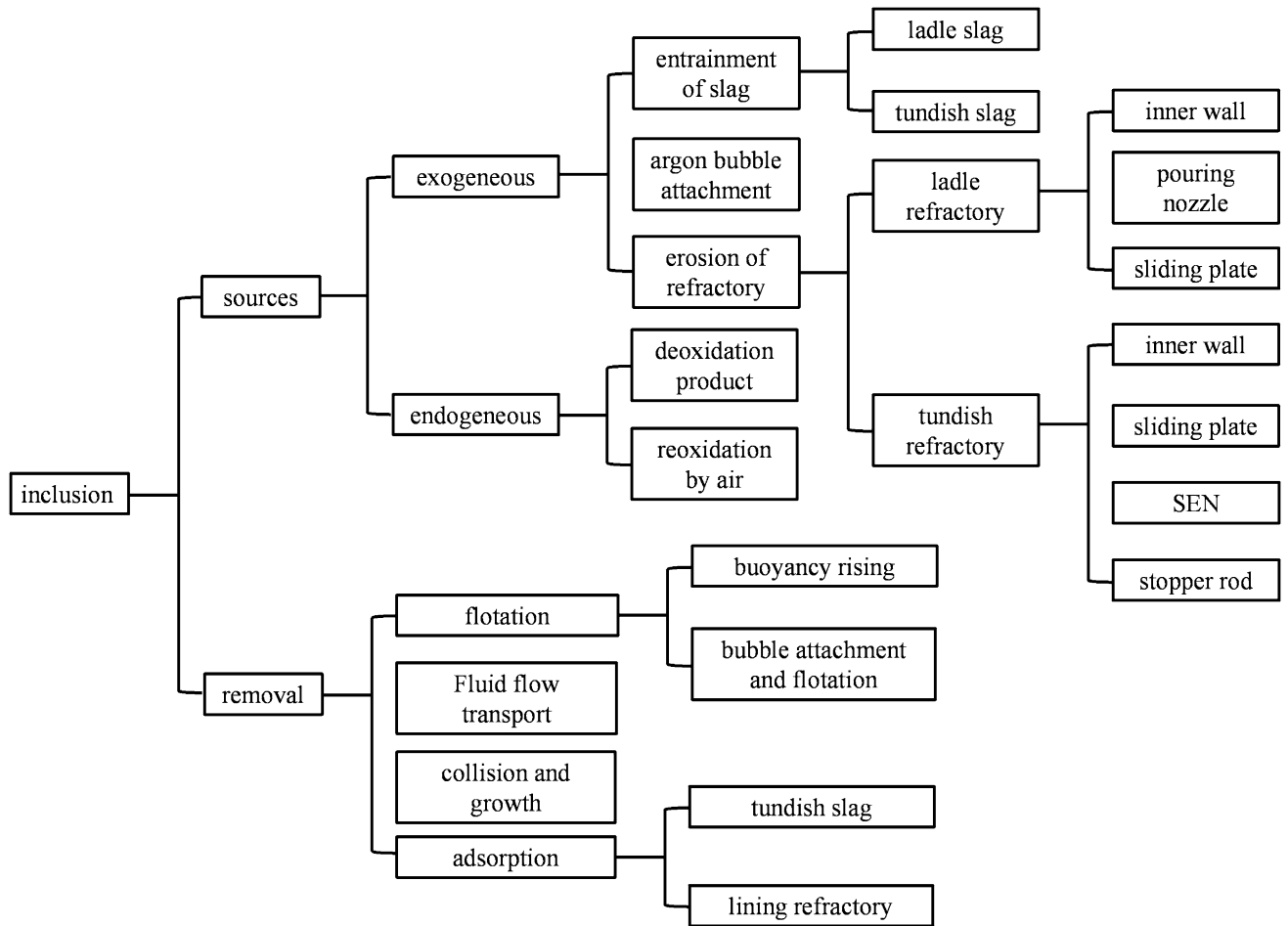
Fig. 1—Sources and removal of inclusions in the molten steel.

The residence time of the molten steel is a key parameter for collision and coalescence of inclusions. In general, the transport equation of the tracer is solved to obtain the residence time distribution (RTD) curve in the tundish. It is expressed by

$$\frac{\partial}{\partial t}(\rho_M \cdot C) + \frac{\partial}{\partial x_i}(\rho_M \cdot \vec{u}_i \cdot C) = \frac{\partial}{\partial x_i}\left(\rho_M \cdot D_{eff}\frac{\partial C}{\partial x_i}\right) \quad [1]$$

$$D_{eff} = D_0 + \frac{\mu_{eff}}{\rho_M \cdot Sc_t} \quad [2]$$

where $\rho_M$ is the density of the molten steel (kg/m$^3$), $u_i$ is the velocity of the molten steel (m/s), $C$ is the concentration of the tracer (kg/m$^3$), $D_{eff}$ is the effective diffusion coefficient (m$^2$/s), $D_0$ is the laminar diffusion coefficient (m$^2$/s), $\mu_{eff}$ is the effective viscosity of the molten steel (Pa s), $Sc_t$ is the turbulent Schmidt number and its value is 0.7.

### B. Collision and Coalescence of Inclusions

The inclusions move together with the molten steel and collide simultaneously with each other in the tundish. Meanwhile, they float up due to the density difference between the molten steel and inclusions. When reaching the top surface, the inclusions have a good opportunity to be absorbed by the slag layer. The transport equation of inclusions in the molten steel is as follows.

$$\frac{\partial}{\partial t}(\rho_M \cdot C_i) + \frac{\partial}{\partial x_j}(\rho_M \cdot \vec{u}_{i,I} \cdot C_i) = \frac{\partial}{\partial x_j}\left(\Gamma\frac{\partial C_i}{\partial x_j}\right) + \rho_M \cdot S_\Phi$$

$$[3]$$

$$U_i = \frac{2g \cdot (\rho_M - \rho_I) \cdot r_i^2}{9\mu_M} \quad [4]$$

$$\bar{d}_{initial} = \left(\frac{\sum_{i=1}^{M} d_i^3 \cdot n_i}{\sum_{i=1}^{M} n_i}\right)^{\frac{1}{3}} \quad [5]$$

$$n_o = \frac{V_T}{\frac{1}{6}\pi \cdot \bar{d}_{initial}^3} \quad [6]$$

**Table I. Reported Studies on the Collision and Removal of Particles From Fluid**

| Year | Researchers | Vessel | Objects | Method | Model | | Collision T | S | B | Gas Effect | References |
|------|-------------|--------|---------|--------|-------|---|---|---|---|-----------|-----------|
| 1956 | Saffman, Turner | — | fluid-drops | numerical integration | — | — | √ | × | × | × | 8 |
| 1974 | Linder | ASEA–SKF | steel-inclusion | numerical calculation | $\kappa - \varepsilon$ | $\mu_t = \rho C_\mu \kappa^2/\varepsilon$ | √ | × | × | × | 45 |
| 1975, 1989 | Nakanishi, Ilegbusi, Szekely | RH tundish | steel-inclusion | E–E | $\kappa - W$ | $\mu_t = \rho\kappa/\sqrt{W}$ | √ | × | × | × | 9,46 |
| | | | | | $\kappa - \varepsilon$ | $\mu_t = \rho C_\mu \kappa^2/\varepsilon$ | | | | | |
| 1993 | Sinha, Sahai | tundish | steel-inclusion | E–E | $\kappa - \varepsilon$ | $\mu_t = \rho C_\mu \kappa^2/\varepsilon$ | √ | × | × | × | 28 |
| 1997, 1999, 2012 | Miki, Xu, Thomas | RH Tundish | steel-inclusion | E–E, E–L | $\kappa - \varepsilon$ | $\mu_t = \rho C_\mu \kappa^2/\varepsilon$ | √ | × | × | √ | 18,30,47 |
| | | — | precipitate particles | PSG | — | — | nucleation + growth | | | | |
| 1999 | Tozawa, Kato | tundish | steel-inclusion | E–E | $\kappa - \varepsilon$ | $\mu_t = \rho C_\mu \kappa^2/\varepsilon$ | √ | √ | √ | × | 11 |
| 2000, 2002, 2003 | Zhang | ASEA–SKF | steel-Al$_2$O$_3$ | E–E | $\kappa - \varepsilon$ | $\mu_t = \rho C_\mu \kappa^2/\varepsilon$ | √ | × | √ | × | 13–16 |
| | | LF | | PSG | — | — | nucleation + growth | | | | |
| | | tundish | | | | | | | | | |
| 2001 | Nakaoka, Taniguchi | CGV | NaCl-PVTL particle | E–E, physical modeling | $\kappa - \varepsilon$ | $\mu_t = \rho C_\mu \kappa^2/\varepsilon$ | √ | × | × | × | 12 |
| 2002 | Sheng | LF | steel-argon-inclusion | E–E | $\kappa - \varepsilon$ | $\mu_t = \rho C_\mu \kappa^2/\varepsilon$ | √ | √ | √ | √ | 20 |
| 2004, 2008 | Zhang, Kwon, Lee | LF | steel-argon-Al$_2$O$_3$ | E–E | $\kappa - \varepsilon$ | $\mu_t = \rho C_\mu \kappa^2/\varepsilon$ | √ | √ | √ | √ | 25,48 |
| 2005 | Wang | mold LF | steel-argon-inclusion | E–E | $\kappa - \varepsilon$ | $\mu_t = \rho C_\mu \kappa^2/\varepsilon$ | √ | √ | √ | √ | 22 |
| 2006 to 2010 | Lei | LF | steel-argon-inclusion | E–E | $\kappa - \varepsilon$ | $\mu_t = \rho C_\mu \kappa^2/\varepsilon$ | √ | √ | √ | √ | 19,21,29,49,50 |
| 2012, 2013 | Felice, Bellot | LF | steel-argon-inclusion | E–E | $\kappa - \varepsilon$ | $\mu_t = \rho C_\mu \kappa^2/\varepsilon$ | √ | √ | × | √ | 31,32 |
| 2013, 2014 | Lou, Zhu | LF | steel-argon-inclusion | E–E | $\kappa - \varepsilon$ | $\mu_t = \rho C_\mu \kappa^2/\varepsilon$ | √ | √ | × | √ | 23,24 |

T: Turbulent collision; S: Stokes collision; B: Brownian collision; √: Consider; ×: Neglect; E: Euler; L: lagrangian; PSG: Particle size grouping method; CGV: Cylindrical glass vessel; PVTL: Polyvinyl-toluene latex.
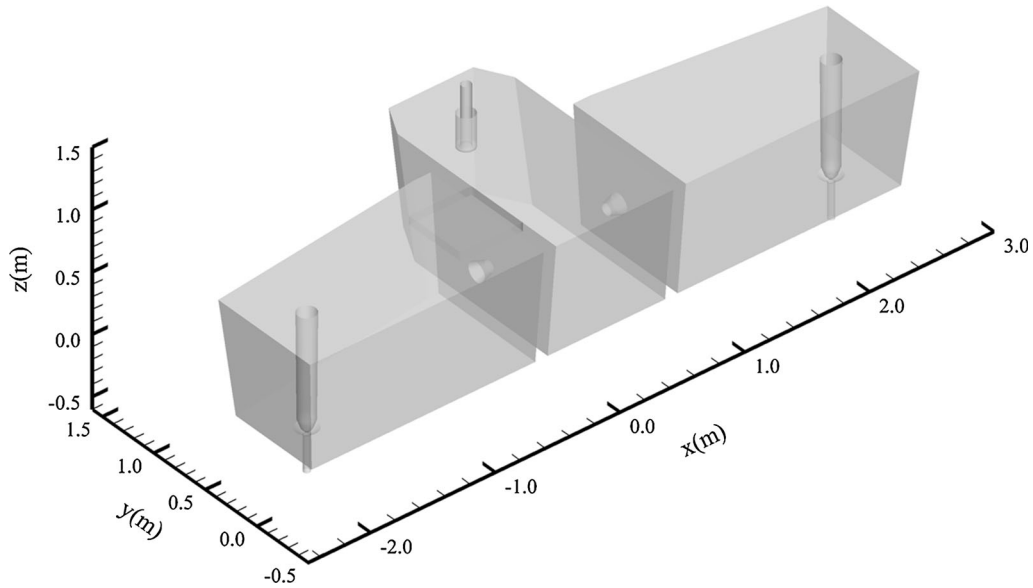
Fig. 2—Schematic of the tundish.

**Table II. Dimensions and Parameters of the Tundish and Properties of the Liquid Steel**

| Parameters | Value | Parameters | Value |
|---|---|---|---|
| Tundish Capacity | 35 t | density of the molten steel | 7020.0 kg/m$^3$ |
| Distance Between the Two Outlets | 4200 mm | viscosity of the molten steel | 0.0067 Pa s |
| Diameter of the Outlet | 50 mm | heat capacity[51] | 750 J/kg K |
| Inner Diameter of the Ladle Shroud | 100 mm | thermal conductivity[51] | 41 W/m K |
| Outer Diameter of the Ladle Shroud | 160 mm | thermal expansion coefficient | $1.0 \times 10^{-4}$ K$^{-1}$ |
| Depth of the Molten Steel | 925 mm | heat flux at the top surface[51] | 15 kW/m$^2$ |
| Submergence Depth of the Ladle Shroud | 250 to 300 mm | heat loss from the bottom wall[51] | 1.4 kW/m$^2$ |
| Diameter of the Stopper Rod | 146 mm | heat loss from long walls[51] | 3.2 kW/m$^2$ |
| Diameter of the Truncated Cone-Shaped Hole | 90 and 160 mm | heat loss from short walls[51] | 3.8 kW/m$^2$ |
| Casting Speed | 0.9 to 1.1 m/min | heat loss from interior walls (weir, baffle, stopper rod)[51] | 1.75 kW/m$^2$ |
| Slab Section | 170 × 1010 mm$^2$ | thickness of wall refractory | 0.2 m |
| Inlet Temperature | 1763 K (1490 °C) | thickness of top slag | 0.05 m |
| Inlet Velocity | 0.81 m/s | thermal conductivity of refractory[51] | 1.5 W/m K |
| Inlet Turbulent Energy | 0.003249 m$^2$/s$^2$ | heat capacity of lining refractory[52] | 1260 J/kg K |
| Inlet Turbulent Energy Dissipation Rate | 0.02025 m$^2$/s$^3$ | outlet pressure | 101325 Pa |

where $C_i$ represents the dimensionless concentration, $C_i = n_i/n_o$, of the $i$th group inclusions in the molten steel, $n_i$ is the number density of the $i$th group inclusions at time $t$(#/m$^3$), and $n_o$ is the initial number density of inclusions with initial average size $\overline{d}_{initial}$ (#/m$^3$). $\overline{d}_{initial}$ is the initial average size of all inclusions (m). $M$ is the maximum group of inclusion size using particle size grouping method. $V_T$ is the initial total volume of inclusions (m$^3$). The variation of $C_i$ reveals the contribution of an increase or decrease in the number density of the $i$th group inclusions to total volume of inclusions. The initial number density of $i$th group was the number density of the $i$th group inclusions after steel refining and was determined by industrial measurement. $\Gamma$ is the diffusion coefficient of inclusions (kg/(m s)). $u_{i,I} = (u_x, u_y, u_z - U_i)$ is the flow velocity of inclusion particles, and $u_x$, $u_y$, and $u_z$ are the velocity of the molten steel in the

tundish in the $x$, $y$, and $z$ directions, respectively. $U_i$ is the stokes floating velocity of the $i$th group inclusions (m/s). $g$ is the acceleration of gravity (m$^2$/s). $\rho_I$ is the density of inclusion particles (kg/m$^3$). $r_i$ is the radius of the $i$th group inclusions (m). $\mu_M$ is the molecular viscosity of the molten steel (Pa s). $S_\Phi$ is the source term of collision and growth of inclusions, which is expressed by[12]

$$\frac{dC_k}{dt} = \frac{2V_{k-1}}{V_k} \cdot \beta(r_{k-1}, r_{k-1}) \cdot C_{k-1} \cdot C_{k-1}$$
$$+ \sum_{i=1}^{k-1} \frac{V_i}{V_k} \cdot \beta(r_i, r_k) \cdot C_i \cdot C_k \qquad [7]$$
$$- \sum_{i=k}^{M} (1 + \delta_{ik}) \cdot \beta(r_i, r_k) \cdot C_i \cdot C_k,$$

**Table III. Hamaker Constants of Particles in Different Liquids Reported in the Literature**

| Year | Researchers | Objects | Hamaker Constant, $\times 10^{20}$ (J) | References |
|------|-------------|---------|------------------------------------------|------------|
| 1980 | Hough and White | polystyrene latex in water | 0.95 | 53 |
| 1988 | Horn et al. | crystal sapphire platelets in an aqueous solution of NaCl | 6.7 | 54 |
| 1996 | Taniguchi et al. | $Al_2O_3$ in liquid iron | 2.3 | 55 |
| | | $SiO_2$ in liquid iron | 3.1 | |
| | | Polystyrene latex in water | 1.2 | |
| | | $SiO_2$ in water | 0.12 | |
| | | $Al_2O_3$ in water | 0.48 | |
| 1997 | Bergstrom | $Al_2O_3$ in vacuum | 15.2 | 56 |
| | | $Al_2O_3$ in water | 3.67 | |
| | | $SiO_2$ in vacuum | 6.50 | |
| | | $SiO_2$ in water | 0.46 | |
| | | $MgO \cdot Al_2O_3$ in water | 2.44 | |
| 2000 | Fernández-Varea et al. | $Si_3N_4$ in water | 4.57 | 57 |
| | | $MgO$ in water | 2.02 | |
| 2001 | Nakaoka et al. | polyvinyl-toluene latex particles in water | 0.8 | 12 |
| 2003 | Leong and Ong | $Al_2O_3$ in water | 0.57 | 58 |
| 2004 | Runkana et al. | hematite in water | 2.4 | 59 |
| 2005 | Bonnefoy et al. | hydrate in water | 0.459 | 60 |
| 2006 | Farmakis et al. | $SiO_2$ in water | 1.02 | 61 |
| 2008 | Zhang et al. | $TiO_2$ in water | 9.1 | 62 |
| | | $Fe_2O_3$ in water | 3.4 | |
| | | $ZnO$ in water | 1.9 | |
| 2009 | Liu et al. | $SiO_2$ in fluidized bed with composition of $SiO_2$-$Al_2O_3$-$Fe_2O_3$ | 6.5 | 63 |
| 2011 | Faure et al. | $SiO_2$ in water | 0.8 | 64 |
| | | $Si_3N_4$ in water | 1.2 | |
| 2013 | Mizoguchi et al. | $Al_2O_3$ in the molten steel | 0.45 | 65 |
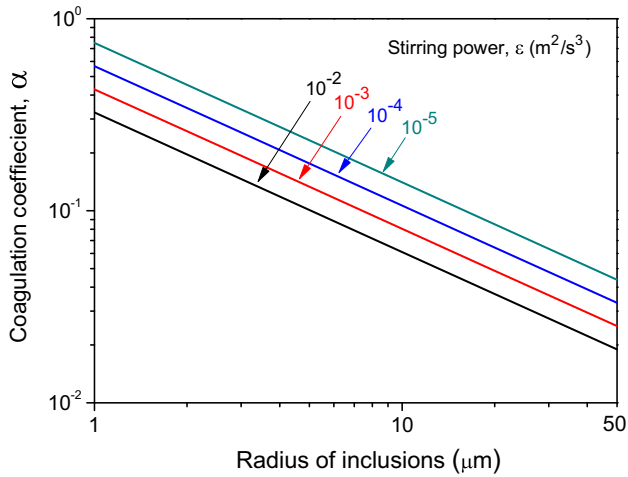


Fig. 3—Effect of turbulent energy dissipation rate on the coagulation coefficient of inclusions, for the case of $2.3 \times 10^{-20}$ J.

where the first two terms are the generation of inclusions and the last term is the sink term of inclusions. $\beta(r_i, r_j)$ is the collision frequency of inclusion particles with radius $r_i$ and $r_j$. $\delta_{ik}$ is the Kronecker's delta function, $\delta_{ik} = 1$ for $i = k$ and $\delta_{ik} = 0$ for $i \neq k$. When $k = 1$ and $k = M$, Eq. [7] is different from that of other groups and the equations are simplified to

$$\frac{dC_1}{dt} = - \sum_{i=1}^{M} (1 + \delta_{i1}) \cdot \beta(r_i, r_1) \cdot C_i \cdot C_1 \qquad [8]$$

$$\frac{dC_M}{dt} = \frac{2V_{M-1}}{V_M} \cdot \beta(r_{M-1}, r_{M-1}) \cdot C_{M-1} \cdot C_{M-1}$$
$$+ \sum_{i=1}^{M-1} \frac{V_i}{V_M} \cdot \beta(r_i, r_M) \cdot C_i \cdot C_M. \qquad [9]$$

There are three mechanisms describing the collision and coalescence of inclusions, including Brownian collision, Stokes collision, and turbulent collision. The collision rate constant of Brownian collision is expressed by[35]

$$\beta_B(r_i, r_j) = \frac{2k_B T}{3\mu_M} \cdot \left( \frac{1}{r_i} + \frac{1}{r_j} \right) \cdot (r_i + r_j), \qquad [10]$$

where $k_B$ is the Boltzmann's constant (J/K), $T$ is the absolute temperature (K).

The collision rate constant of Stokes collision is represented by[36]

$$\beta_S(r_i, r_j) = \frac{2\pi g(\rho_M - \rho_I)}{9\mu_M} \cdot \left| r_i^2 - r_j^2 \right| \cdot (r_i + r_j)^2. \qquad [11]$$

The turbulent collision rate constant between inclusion particles with radius $r_i$ and $r_j$, $\beta_T(r_i, r_j)$, is given as below.[8,14]

$$\beta_T(r_i, r_j) = 1.3\alpha \cdot \sqrt{\pi} \cdot (r_i + r_j)^3 \cdot (\varepsilon/v)^{1/2}, \qquad [12]$$

where $\varepsilon$ and $v$ are the turbulent energy dissipation rate (m²/s³) and the kinematic viscosity of the molten steel

$(m^2/s)$, respectively. $\alpha$ is the coagulation coefficient and it is calculated by the following equation[12]

$$\alpha = 0.738 \left( \frac{\mu_M \cdot (\min(r_i, r_j))^3 \cdot (\varepsilon/v)^{1/2}}{A_{131}} \right)^{-0.242}, \quad [13]$$
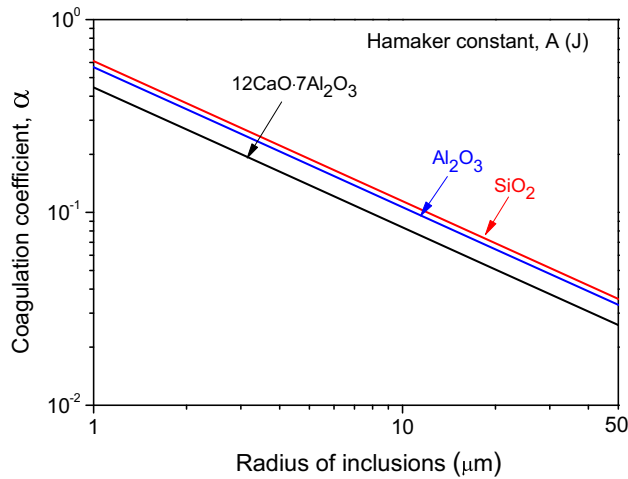


Fig. 4—Effect of Hamaker constants on the coagulation coefficient of inclusions, for the case of $10^{-4}$ m$^2$/s$^3$.

where $A_{131}$ is the effective Hamaker constant (J). Table III shows the Hamaker constants in different mediums. The coagulation coefficient depends on the size of inclusions, turbulent energy dissipation rate, and Hamaker constant. It decreases with increasing the size of inclusions and turbulent energy dissipation rate, as shown in Figure 3. But for Hamaker constants, it is closely related to the composition of inclusions in the molten steel. As shown in Figure 4, the coagulation coefficient of $12CaO \cdot 7Al_2O_3$ inclusions is significantly smaller than that of $Al_2O_3$ and $SiO_2$ inclusions.

## C. Boundary and Initial Conditions

The inlet velocity at the tundish was calculated according to the casting speed and the cross section area of the continuous casting slab. The top surface of the tundish was assumed as a free surface with a zero shear stress. The pressure was set to a constant atmospheric pressure at the outlet. The heat flux or loss in Table II was chosen to model the energy transport at the top surface, the bottom and side walls. The initial concentration of inclusions in each group was chosen to patch within the entire tundish at the initial time. A no-flux condition for inclusions was assumed at the walls.
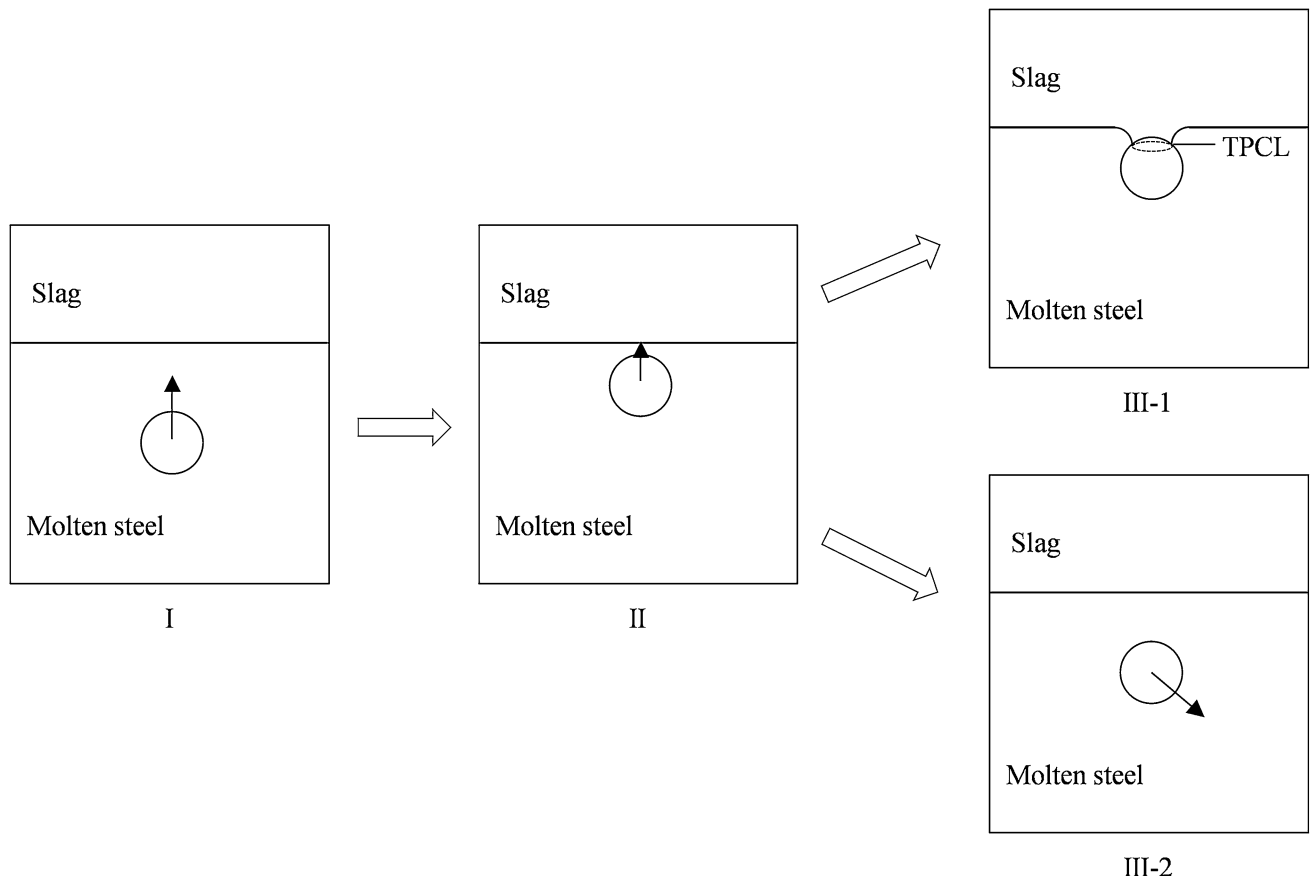


Fig. 5—Schematic of the interaction steps between the molten steel, slag, and inclusion.
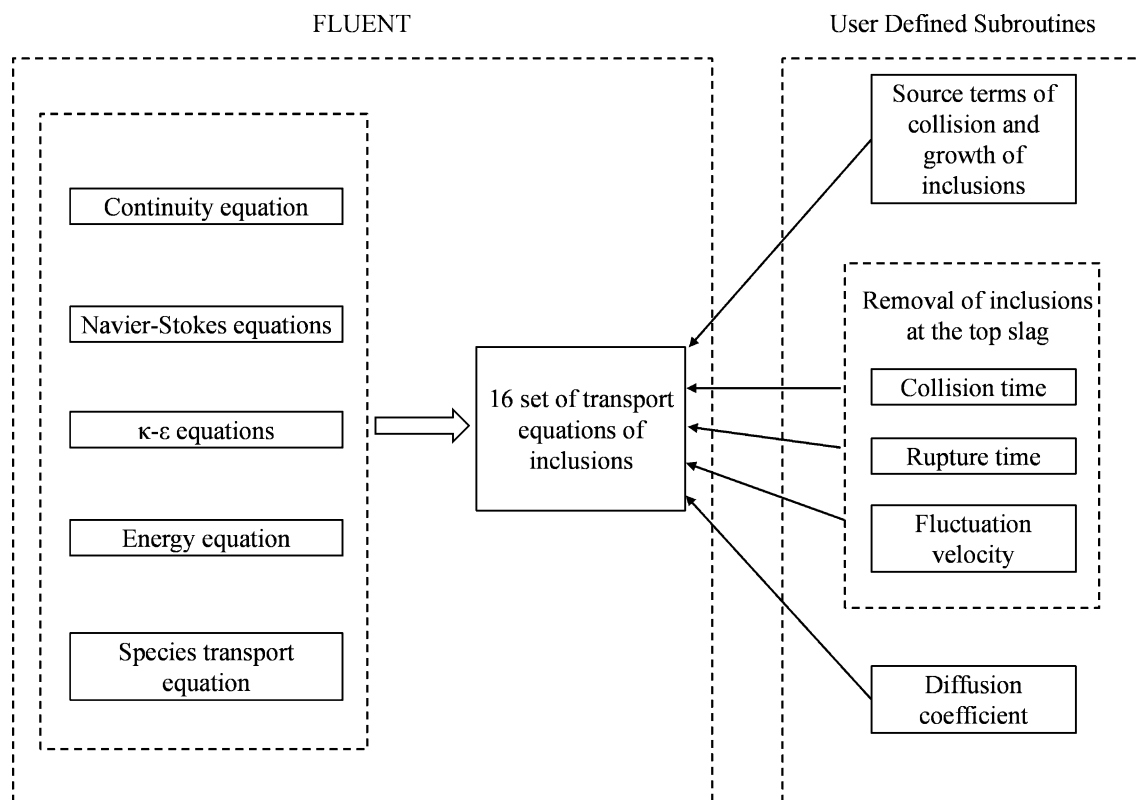
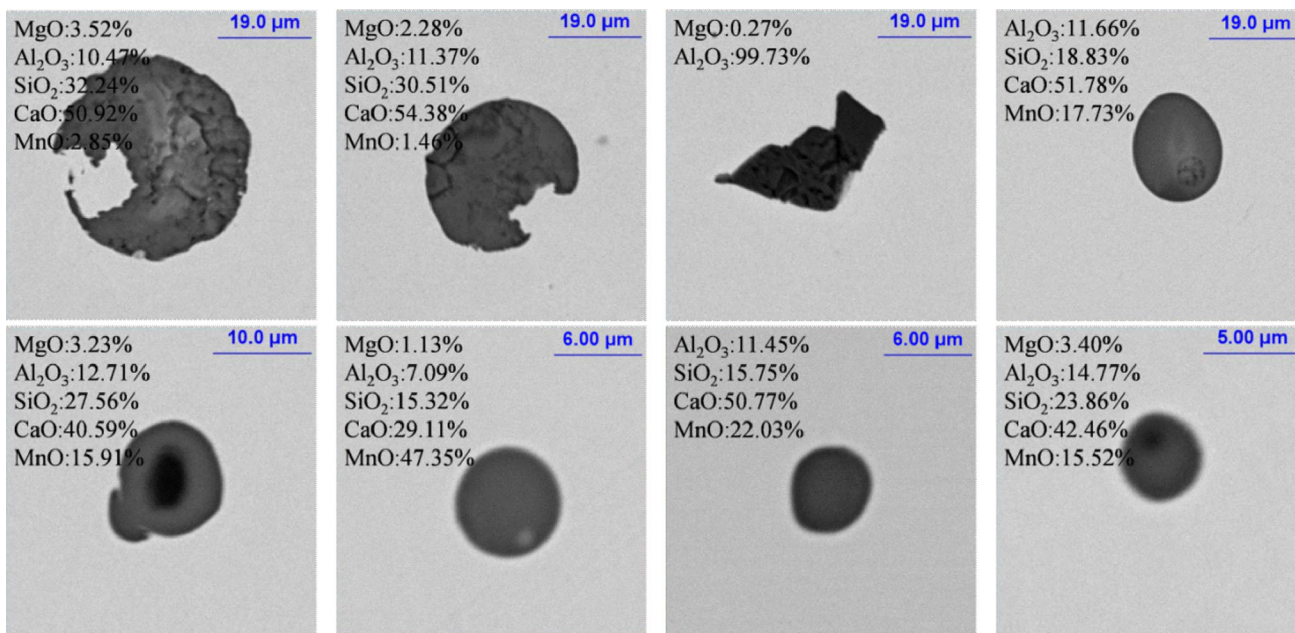Fig. 6—Flow chart of mathematical models.



Fig. 7—Typical morphology of inclusions in steel samples.

The removal of inclusions at the interface between the molten steel and slag was a very complicated process. But so far there were no appropriate model to describe it. In 2000, Zhang and Taniguchi[37] reviewed the interaction process between a gas bubble and an inclusion particle, including the approach of a bubble to an inclusion, formation of a thin liquid film, collision and sliding, film rupture and the removal of the inclusion attaching to the bubble. In the current study, similar processes were used to define the removal of inclusions from the top slag, as shown in Figure 5:

I. approaching of the inclusion to the slag–steel interface
II. collision of the inclusion with the interface and the formation of a thin steel film between the slag and the inclusion;
III. drainage and rupture of the thin film and the formation of a steady three phase contact line (TPCL);
IV. the inclusion backs to the bulk since no rupture of the film occurs during the collision between the inclusion and the slag.

There were two key parameters: collision time $t_C$, the time of oscillation of the inclusion following initial collision with the interface; rupture time $t_F$, the period elapsing from the drainage of the film between slag and the inclusion to the rupture of the film.

**Table IV.  Average Density of Inclusions**

| Composition | Mass Fraction (pct) | Density (kg/m³) | Average Density (kg/m³) |
|---|---|---|---|
| MnO | 62.99 | 5450 | 4413 |
| SiO₂ | 19.21 | 2500 | |
| CaO | 11.85 | 3350 | |
| Al₂O₃ | 5.91 | 3970 | |
| MgO | 0.04 | 3580 | |

**Table V.  Parameters of MnO-SiO₂-CaO-Al₂O₃-MgO Inclusions in the Molten Steel**

| Parameters | Value |
|---|---|
| Hamaker Constant, ×10²⁰ (J) | 2.3[55] |
| Density of the Inclusion (kg/m³) | 4413 |
| Interfacial Tension Between the Molten Steel and Slag (N/m) | 1.257[66] |
| Viscosity of the Molten Steel (Pa s) | 0.0067 |
| Contact Angle at the Molten Steel and Slag Interface (deg) | 6[67] |

A random number was introduced to model in order to consider the effect of the turbulence fluctuation on the interaction between the inclusion and the slag. The relative velocity between the slag and the inclusion is given by

$$u_R = U_i + u_z', \quad [14]$$

where $u_z'$ is the random velocity fluctuation in the vertical direction at the top surface (m/s), represented by

$$u_z' = \xi \cdot \sqrt{\frac{2}{3}k}, \quad [15]$$

where $\xi$ is a normally distributed random number, which is generated in each time step. $k$ is the turbulent kinetic energy (m²/s²).

Zhang and Taniguchi[37] compared different models of the collision time and pointed out that the following equation[38] was to calculate the collision time. The expression is listed by

$$t_C = \left(\frac{d_I^3 \cdot \rho_I}{12\sigma_{MS}}\right)^{1/2} \cdot \left\{\pi + 2\arcsin\left[1 + \frac{12u_R^2\sigma_{MS}\rho_I}{d_I^3 g^2(\rho_I - \rho_M)^2}\right]^{-\frac{1}{2}}\right\}, \quad [16]$$

where $d_I$ is the diameter of inclusions (m), $\sigma_{MS}$ is the interfacial tension between the molten steel and the slag (N/m). The rupture time of the film formed between the slag and the inclusion particle is expressed by[39]

$$t_F = \frac{3}{64}\mu_M \frac{\phi^2}{m\sigma_{MS}h_{Cr}^2}d_I^3 \quad [17]$$

$$\phi = \arccos\left\{1 - 1.02 \cdot \left(\frac{\pi d_I\rho_I u_R^2}{12\sigma_{MS}}\right)^{\frac{1}{2}}\right\}, \quad [18]$$
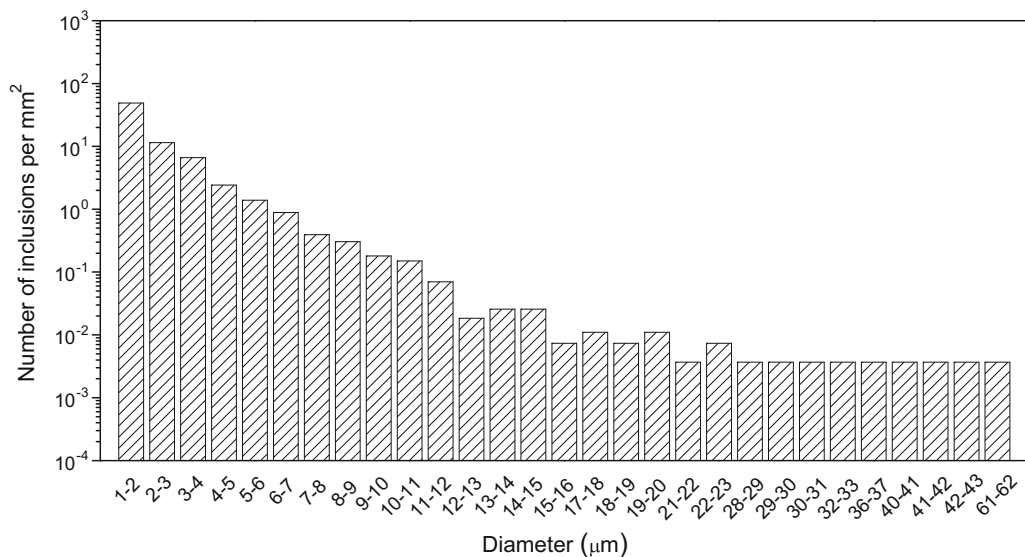


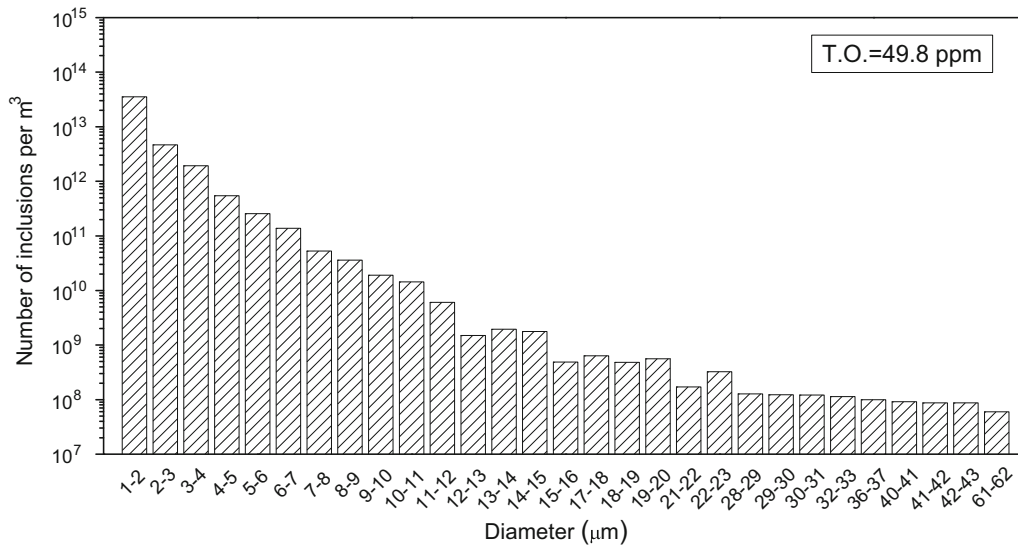Fig. 8—Two-dimensional size distribution of inclusions in the steel sample after steel refining.

Fig. 9—Three-dimensional size distribution of inclusions converted from the original two-dimensional observation data.

**Table VI. Size Distribution of Inclusions**

| Group | Diameter ($\mu$m) | Characteristic Diameter ($\mu$m) | Number Density (#/m$^3$) | Dimensionless Initial Concentration |
|---|---|---|---|---|
| 1 | <1.18 | 1.00 | $1.32 \times 10^{13}$ | $2.93 \times 10^{-1}$ |
| 2 | 1.18 to 1.60 | 1.36 | $1.74 \times 10^{13}$ | $3.86 \times 10^{-1}$ |
| 3 | 1.60 to 2.17 | 1.84 | $7.74 \times 10^{12}$ | $1.72 \times 10^{-1}$ |
| 4 | 2.17 to 2.95 | 2.50 | $3.61 \times 10^{12}$ | $8.02 \times 10^{-2}$ |
| 5 | 2.95 to 4.00 | 3.39 | $2.04 \times 10^{12}$ | $4.53 \times 10^{-2}$ |
| 6 | 4.00 to 5.43 | 4.61 | $6.57 \times 10^{11}$ | $1.46 \times 10^{-2}$ |
| 7 | 5.43 to 7.37 | 6.25 | $2.98 \times 10^{11}$ | $6.63 \times 10^{-3}$ |
| 8 | 7.37 to 10.00 | 8.48 | $8.10 \times 10^{10}$ | $1.80 \times 10^{-3}$ |
| 9 | 10.00 to 13.57 | 11.51 | $2.30 \times 10^{10}$ | $5.11 \times 10^{-4}$ |
| 10 | 13.57 to 18.41 | 15.63 | $3.29 \times 10^{9}$ | $7.32 \times 10^{-5}$ |
| 11 | 18.41 to 24.99 | 21.21 | $1.04 \times 10^{9}$ | $2.31 \times 10^{-5}$ |
| 12 | 24.99 to 33.92 | 28.78 | $5.11 \times 10^{8}$ | $1.14 \times 10^{-5}$ |
| 13 | 33.92 to 46.04 | 39.06 | $3.76 \times 10^{8}$ | $8.37 \times 10^{-6}$ |
| 14 | 46.04 to 62.49 | 53.02 | $6.93 \times 10^{7}$ | $1.54 \times 10^{-6}$ |
| 15 | 62.49 to 84.80 | 71.95 | 0.00 | 0.00 |
| 16 | 84.80 to 115.10 | 97.66 | 0.00 | 0.00 |

where $h_{Cr}$ is the critical thickness of liquid film for film rupture (m). $m$ is a constant, equal to 1 for inclusion particles. Schulze and Birzer[40] regressed an empirical expression between critical film thickness, surface tension, and contact angle

$$h_{Cr} = 2.33 \times 10^{-8}[1000 \cdot \sigma_{MS}(1 - \cos \theta)]^{0.16}. \quad [19]$$

By the discussions above, the removal condition of inclusions to the top slag is as follows: (i) If $u_R \leq 0$, where a positive sign means upwards, the inclusion will not reach the slag thus can not be absorbed. (ii) If $u_R > 0$ and $t_C < t_F$, the thin film is not able to rupture during the collision between the slag and the inclusion so that the inclusion will rebound from the slag and not be removed. (iii) If $u_R > 0$ and $t_C \geq t_F$, the thin film is ruptured during collision between the inclusion and the slag so that a TPCL is formed and the

inclusion is steadily absorbed to the slag and is removed from the molten steel. The discussion above and the flux of inclusions to the slag can be summarized by

$$\text{Flux} = \begin{cases} -\rho_M \cdot u_R \cdot C_i & u_R > 0, t_C \geq t_F \\ 0 & u_R > 0, t_C < t_F \\ 0 & u_R \leq 0 \end{cases} \quad [20]$$

### D. Computational Procedure

The models and equations above were solved by combining the authors' user-defined subroutines with the commercial CFD software (Fluent version 14.0).[41] The flow chart of the mathematical models is given in Figure 6. The optimum number of mesh cells for the current tundish was approximately 330,000. The

non-equilibrium wall function is used to model the turbulence characteristics in the near-wall region. The convergence criterion for the continuity, momentum,



Fig. 10—Three-dimensional size distribution of inclusions by particle size grouping method.

turbulent kinetic energy and its dissipation rate was set to $10^{-5}$, and was $10^{-6}$ and $10^{-4}$ for energy equation and the concentration equation of inclusions, respectively. The SIMPLE scheme was used for the pressure–velocity coupling. The time step was 0.1 second. All computations were performed with a Windows 7 PC with Intel 3.4 GHz CPU and 8 GB RAM. The flow field, temperature distribution, and residence time distribution of the molten steel in the tundish were calculated first, and then the equation of inclusions was computed. The computation time was 4 days.

## III. INDUSTRIAL MEASUREMENT OF INCLUSIONS AFTER STEEL REFINING AND IN CONTINUOUS CASTING TUNDISH

Steel and slag samples were taken from an industrial plant and the steel grade was a 200-series stainless steel. During ladle refining, 65 kg Si-Fe and 700 kg electrolytic
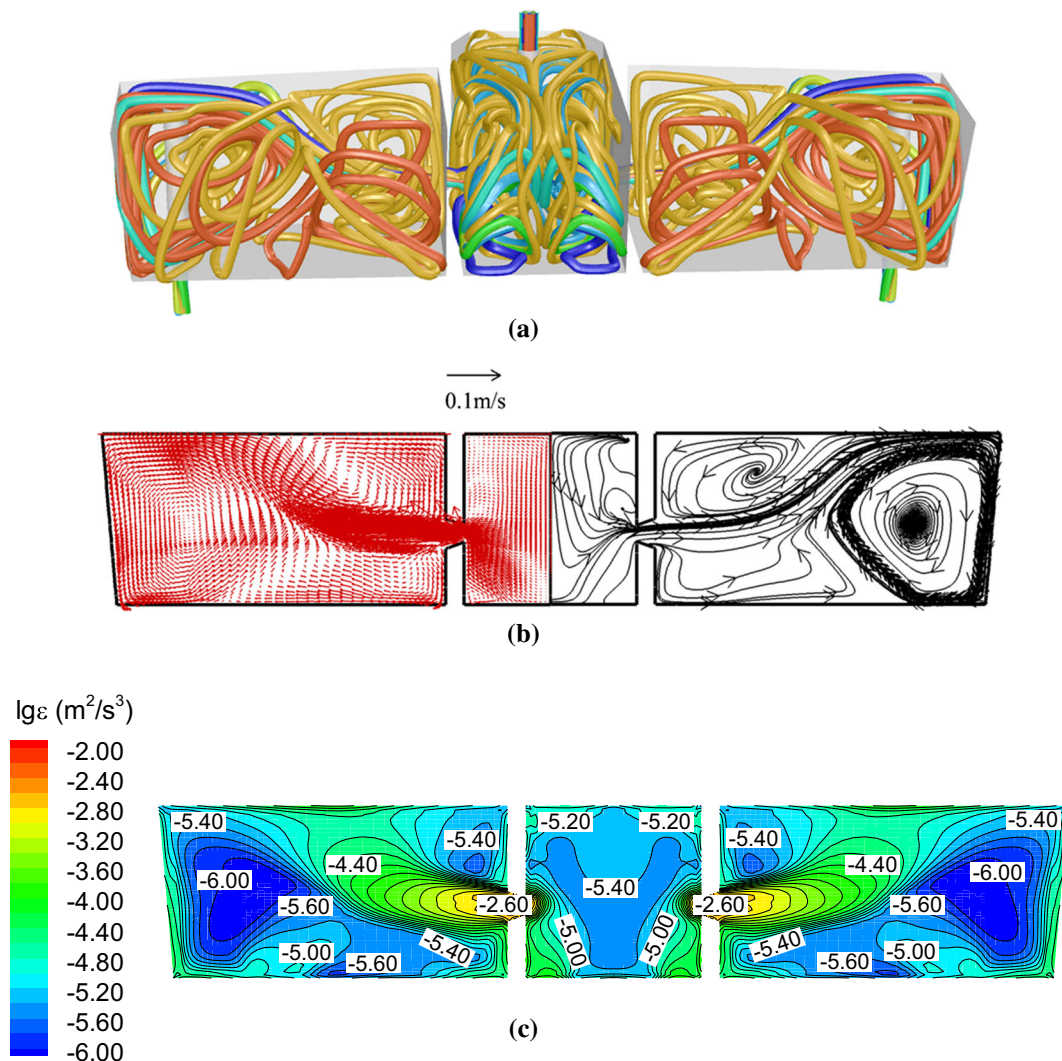


Fig. 11—Predicted distribution in the tundish of (a) streamline in a global view; (b) velocity and streamline in the plane $y = 205$ mm; (c) turbulent energy dissipation rate in the plane $y = 205$ mm.
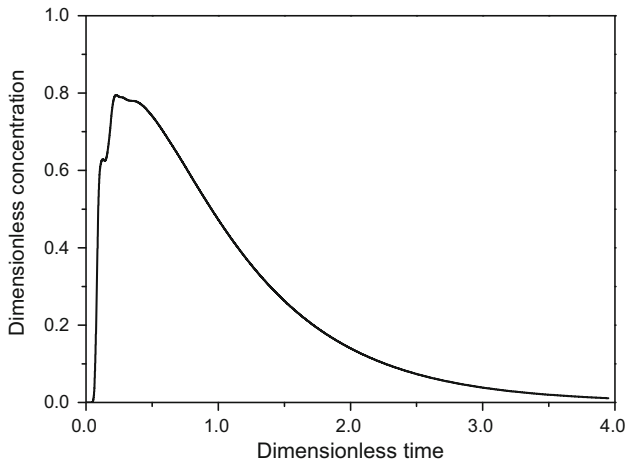
Fig. 12—Residence time distribution of the molten steel.

Mn were added to deoxidize and adjust the composition. Steel and slag samples were taken at the end of steel refining and 300 mm below the top surface of the pouring zone and above the outlet in the tundish. Eight samples were taken at each position in the tundish within 40 minutes.

Inclusions in steel samples were detected using automated SEM–EDS system, called ASPEX1020 system.[42,43] The rotating chord algorithm was used to measure the particle. The beam energy was set at 20 kV and the working magnification was 450. Inclusions with size >1 $\mu$m on an approximate 270 mm$^2$ area of the cross section of each steel sample were obtained. The amount, morphology, size, and composition of inclusions were evaluated. The detected inclusions at the end of ladle refining were defined as the initial conditions in the tundish. The diameter of inclusions was in the range from 1.00 to 61.35 $\mu$m.

Table VII.    Results of Residence Time Distribution

|  | $t_{th}$ (s) | $t_{min}$ (s) | $t_{peak}$ (s) | $t_m$ (s) | $V_t$ (pct) | $V_m$ (pct) | $V_d$ (pct) |
|---|---|---|---|---|---|---|---|
| Outlet | 784 | 51.5 | 61.5 | 625 | 7.2 | 72.5 | 20.3 |



(a)



(b)



(c)
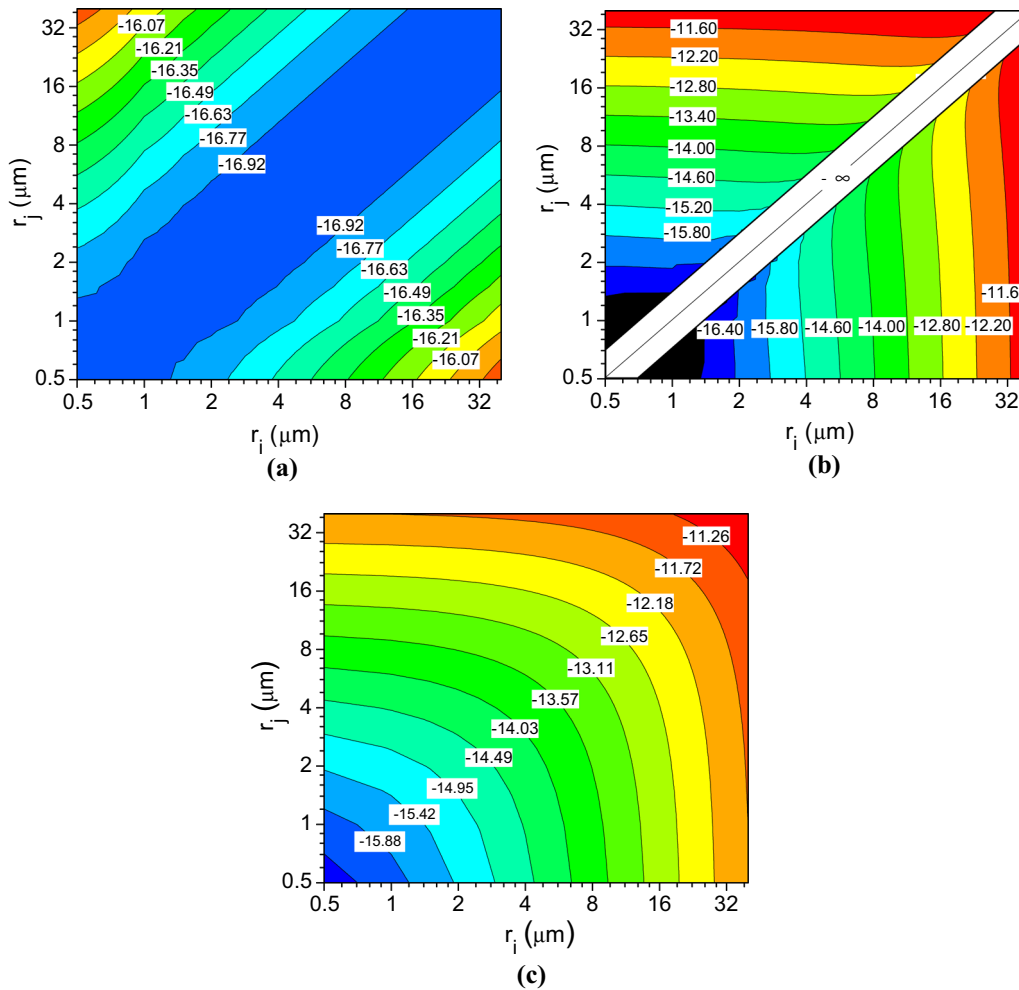
Fig. 13—Collision rate constants of three different mechanisms. (a) Brownian collision: $\log_{10}(\beta_B(r_i, r_j))$; (b) stokes collision: $\log_{10}(\beta_S(r_i, r_j))$; (c) turbulent collision: $\log_{10}(\beta_T(r_i, r_j))$.

Figure 7 shows typical morphology of inclusions in steel samples. Inclusions were mainly spherical MnO-SiO$_2$-CaO-Al$_2$O$_3$, including a small amount of MgO. There also existed some irregular-shaped pure Al$_2$O$_3$ inclusions. Besides, the average compositions of inclusions are MnO 62.99 pct, CaO 11.85 pct, SiO$_2$ 19.21 pct, Al$_2$O$_3$ 5.91 pct, MgO 0.04 pct, as shown in Table IV. Consequently, the average density of inclusions in the molten steel is 4413 kg/m$^3$. Table V shows the essential parameters related to the molten steel, slag and inclusions, including the Hamaker constant, interfacial tension, viscosity and contact angle.

The number density of inclusions is determined by

$$n_{2D} = \frac{n_i}{A_0},$$ [21]

where $n_{2D}$ is the number of inclusions per mm$^2$ of steel surface area under two-dimensional microscope observation, as shown in Figure 8. $A_0$ is the scanning area (mm$^2$).
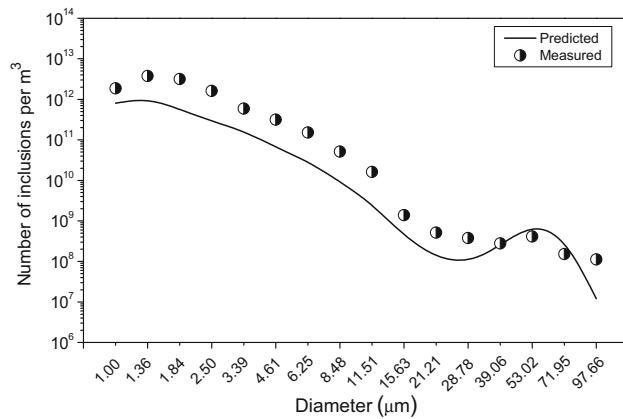


Fig. 14—Variation of number density of inclusions 300 mm below the surface and above the outlet at 10 min casting.
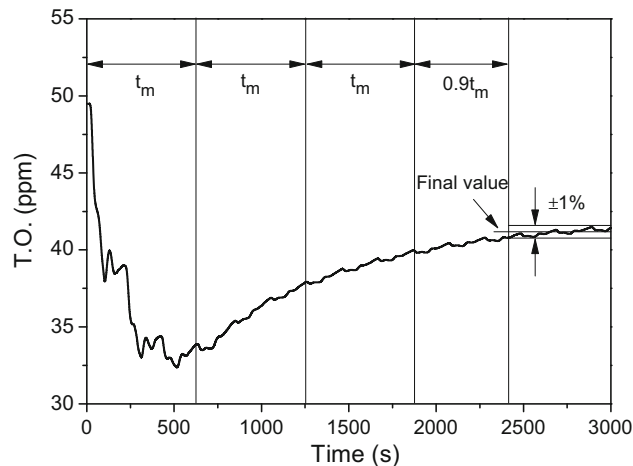


Fig. 15—Variation of the total oxygen at the outlet converted from mass concentration of inclusions (final value: the average total oxygen from 2500 to 3000 s).

According to the previous investigation,[44] the two-dimensionless size distribution can be converted into the three-dimensional size distribution using Eq. [22] and is shown in Figure 9

$$n_{3D} = \frac{n_{2D}}{d_{I,2D}} \times 10^{12},$$ [22]

where $n_{3D}$ is the number of inclusions per m$^3$ of steel volume. $d_{I,2D}$ is the inclusion diameter under two-dimensional (2D) microscope observation ($\mu$m). The 2D diameter is usually smaller than its 3D diameter because the observed section surface is rarely just across the diameter section of the spherical inclusion. Hence, the observed 2D steel cleanliness somehow underpredicts the fraction of inclusions in the steel.

The size of inclusions was divided into 16 groups and the volume ratio from one group to the next was assumed to be 2.5 using particle size grouping method, as shown in Eq. [23]. The statistical characteristic diameter, number density, and dimensionless concentration of inclusions of each group are shown in Table VI. The value of $n_o$ and $\overline{d}_{initial}$ were $4.50 \times 10^{13}$ #/m$^3$, 2.27 $\mu$m, respectively. Furthermore, inclusions smaller than 1 $\mu$m were ignored because the total oxygen converted from these small inclusions was below 1 ppm

$$R_v = \frac{V_{i+1}}{V_i} = 2.5.$$ [23]

The number of inclusions decreased consistently with increasing size, as shown in Figures 8 and 9. There were $4.3 \times 10^{13}$ inclusions smaller than 14 $\mu$m/m$^3$ of steel. Meanwhile, there were $5.3 \times 10^9$ inclusions larger than 14 $\mu$m/m$^3$ steel. According to Table IV, the total mass concentration of all inclusions was 162.6 ppm, corresponding to 49.8 ppm total oxygen in the steel. The converted results using particle size grouping method were slightly different from original ones, as shown in Figure 10. The total number density of inclusions smaller than 13.57 $\mu$m was $4.5 \times 10^{13}$ #/m$^3$ and was
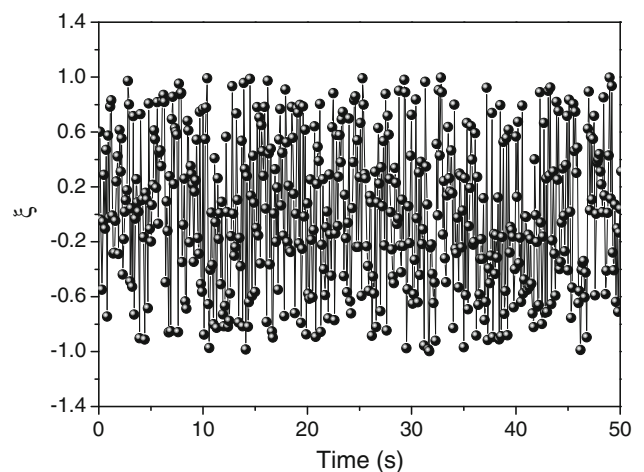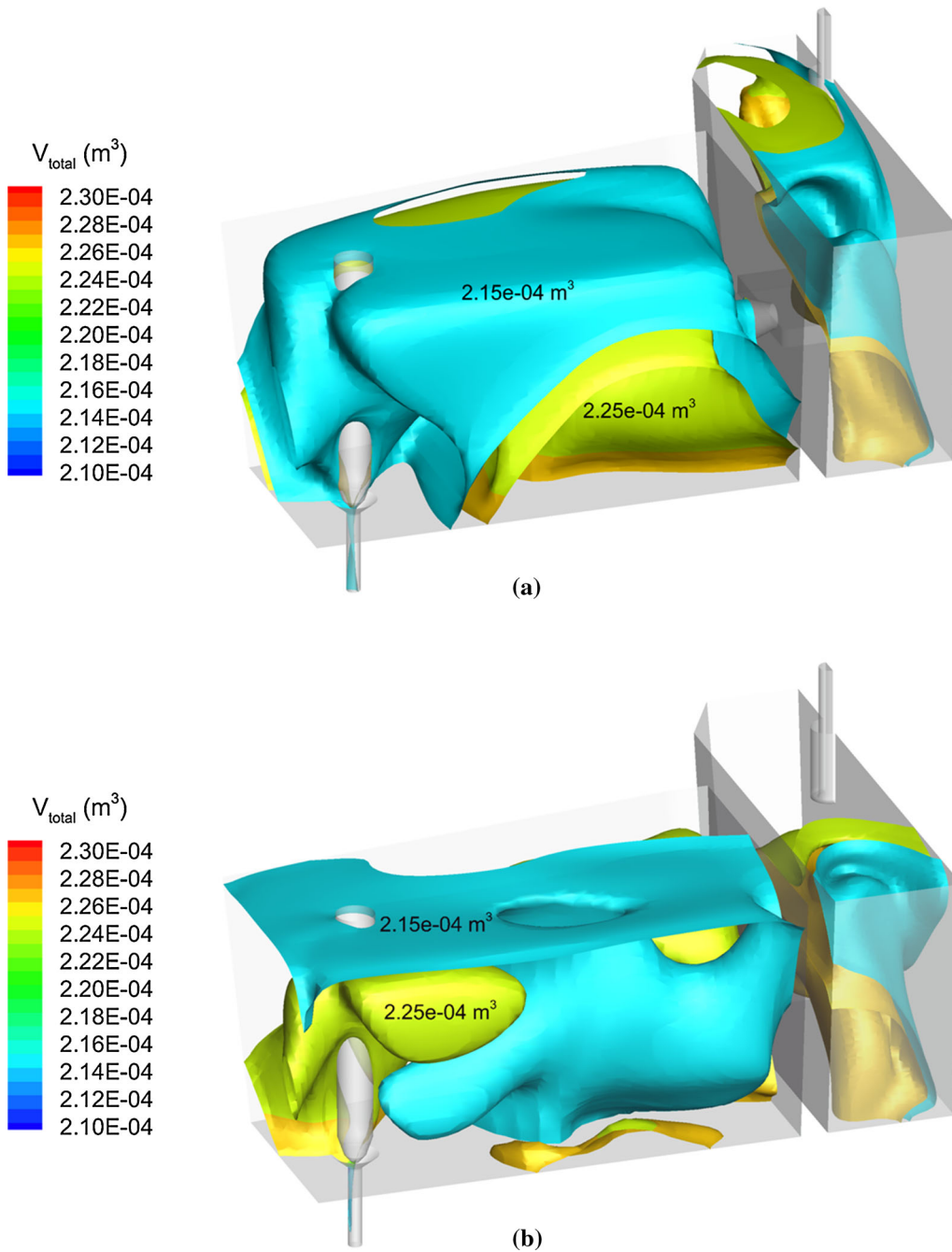


Fig. 16—Variation of the random number with time.

Fig. 17—Distribution of total volume of inclusions in the tundish at two different moments. (*a*) 100 s; (*b*) 125 s.

$5.2 \times 10^9$ #/m$^3$ for >13.57 $\mu$m inclusions. Besides, the total oxygen was 49.5 ppm, equivalent to the original value. Therefore, the groups and volume ratio were appropriate to calculate collision and coalescence of inclusions.

## IV. FLUID FLOW OF MOLTEN STEEL IN THE TUNDISH

Figure 11 shows the distribution of fluid flow velocity, streamline, and turbulent energy dissipation rate in the tundish. The molten steel from the ladle shroud firstly impinged the bottom of the tundish, and then flowed upwards along the inside wall of the weir. The strong turbulence was effectively controlled within the inlet zone using the weir. Then the molten steel flowed towards the truncated cone-shaped hole in the weir after a complicated spiral flow. The molten steel from the hole directly flowed upwards, reached the top surface, and then flowed downwards along the short wall, reached the bottom and then again flowed upwards, which provided a long residence time for inclusions to float up and be assimilated by the cover slag. Two big
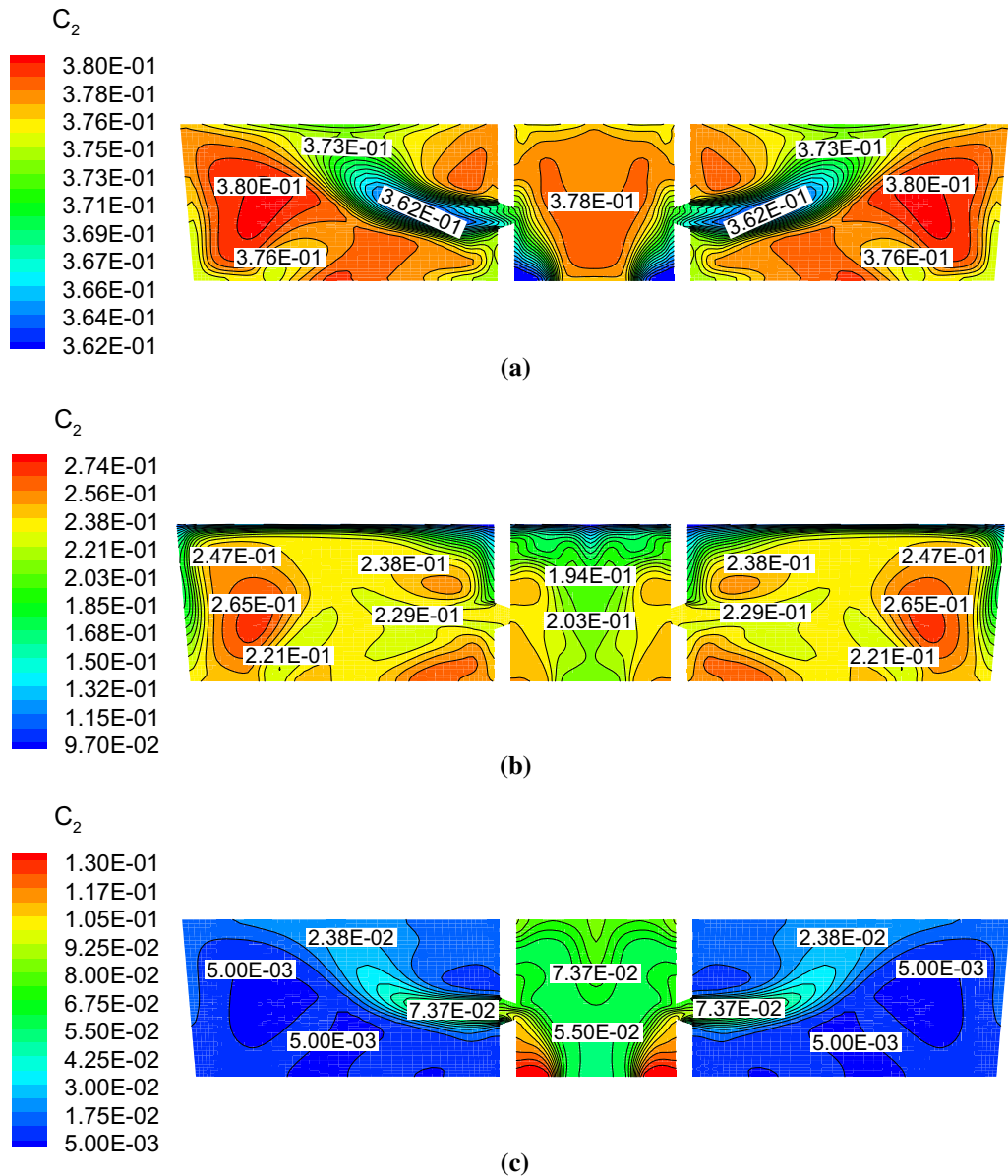
**(a)**



**(b)**



**(c)**

Fig. 18—The concentration distribution of 1.36 μm inclusions at different times. (*a*) 5 s; (*b*) 75 s; (*c*) 2440 s.

recirculation zones existed near the left and right narrow walls. Besides, the velocity direction of the molten steel changed after reaching a certain height, and then flowed towards the weir. Finally, the molten steel flowed towards the outlet after a long moving path length.

The value of the turbulent energy dissipation rate in the outer area of the hole in the weir and at the bottom corner of the inlet zone in Figure 11(c) was significantly larger than that of other zones. The maximum value was about −2.60. However, it was much smaller in two big recirculation zones and the minimum value was about −6.00. According to Eq. [12], the collision rate constant of turbulent collision was proportional to the turbulent energy dissipation rate. It was of great importance for collision and coalescence of inclusions. Therefore, it improved inclusion growth by forced coagulation in

above zones, and the collision and coalescence of inclusions should be far stronger than that in other zones. However, it should be much weaker in two big recirculation zones.

Due to the symmetry of the geometric model, only one residence time distribution (RTD) curve at the outlet was calculated. It was represented in a dimensionless form, as shown in Figure 12. The time when the dimensionless time was equal to 2 was the mean residence time, as listed in Table VII. The minimum and peak concentration residence time were 51.5 and 61.5 seconds, respectively. The mean residence time was 625 seconds, during which the collision and removal of inclusions occurred continuously. After that, the inclusions flowed into the mold together with the molten steel.
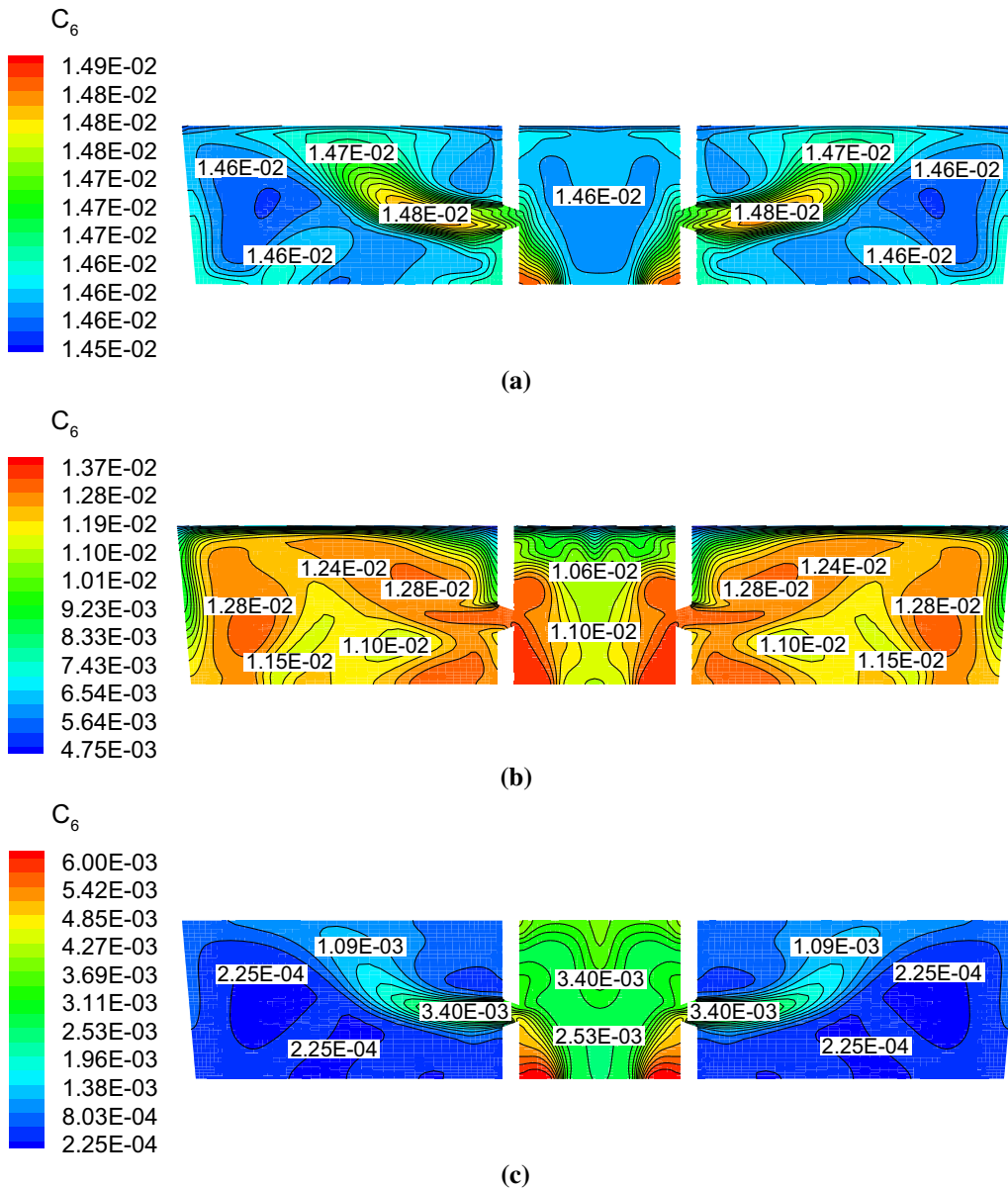
Fig. 19—The concentration distribution of 4.61 $\mu$m inclusions at different times. (*a*) 5 s; (*b*) 75 s; (*c*) 2440 s.

## V. INCLUSION GROWTH AND REMOVAL IN THE TUNDISH

### A. *Discussion on Collision Rate Constant*

Figure 13 shows the collision rate constants of three different mechanisms, expressing in the common logarithmic form ($\log_{10} \beta(r_i, r_j)$). Based on the velocity field, the volume-weighted average turbulent energy dissipation rate of the entire tundish was $1.4 \times 10^{-4}$ m$^2$/s$^3$. It was used to calculate the collision rate constant of turbulent collision. As shown in Figure 13(b), the collision rate constant of Stokes collision was almost the same as that of turbulent collision when small-sized inclusions collided with big size ones. But it was zero for two inclusions with a same radius. Because they have a same floating velocity and it is impossible to contact

with each other. In addition, the collision rate constant of Brownian collision was less than $10^{-16}$ m$^3$/s and greatly lower than the Stokes and turbulent collision rate constants. Hence, the Stokes and turbulent collision were the dominant factors for collision and coalescence of inclusions in the tundish.

### B. *Comparison Between Computation and Measurement*

To validate the calculated results, inclusions in the steel sample taken at 10 minutes casting and 300 mm below the surface and above the outlet were scanned and analyzed. The total scanning area was 183 mm$^2$ and the diameter of inclusions was in the range from 1.00 to 108.63 $\mu$m. The calculated dimensionless
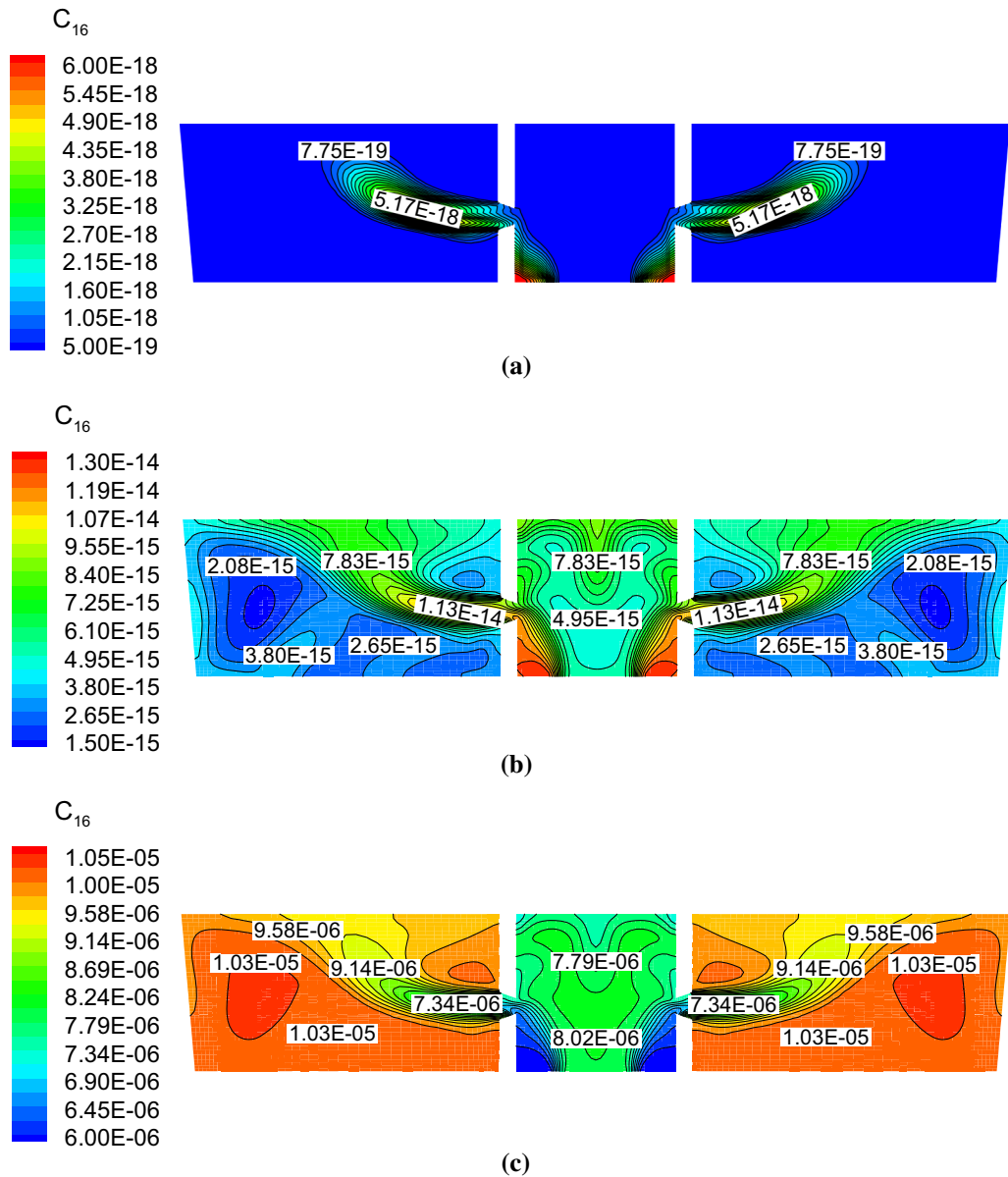
Fig. 20—The concentration distribution of 97.66 $\mu$m inclusions at different times. (*a*) 5 s; (*b*) 75 s; (*c*) 2440 s.

concentration of inclusions in each group was exported at 10 minutes, corresponding to the same sampling position. There were a certain discrepancy between the measured and predicted results for small-sized inclusions, such as from 1.36 to 11.51 $\mu$m, as shown in Figure 14. The discrepancy gradually decreased with increasing size of inclusions. For 97.66 $\mu$m inclusions, the measured results were larger than the predicted ones because detecting a large-sized inclusion is very difficult and its statistical amount has uncertainties in the detected fields. When the scanning area is large enough, the discrepancy will be eliminated. In summary, the predicted results showed a certain agreement with the measured ones, indicating that the current mathematical model can be used to accurately simulate collision and coalescence of inclusions.

## C. Discussion on the Steady State

Figure 15 shows the variation of total oxygen converted from mass concentration of inclusions at tundish outlet. The time when the total oxygen reached ±1 pct of the final value was defined as the equilibrium time ($t_e$), at which the concentration of inclusions in the tundish remained stable. The final total oxygen was the average value of total oxygen from 2500 to 3000 seconds. The total oxygen at the outlet firstly descended in a fluctuation tendency and then gradually increased due to the inflow of inclusions in the inlet, and finally reached the steady state. The random number during 50 seconds is shown in Figure 16. It was clearly shown that the equilibrium time was about 2440 seconds, equivalent to 3.9 times of the mean residence time, as shown in Eq. [24].
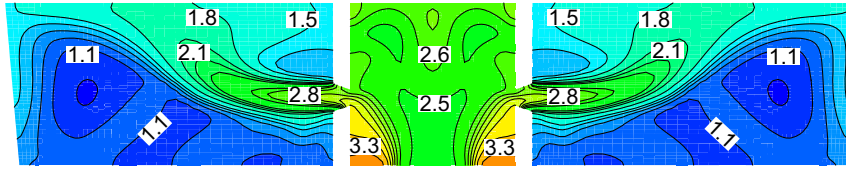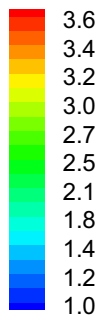
$$t_e = 3.9 \cdot t_m, \qquad [24]$$

Fig. 22—Distribution of average diameter of inclusions in the plane $y = 205$ mm when reaching the steady state (2440 s).
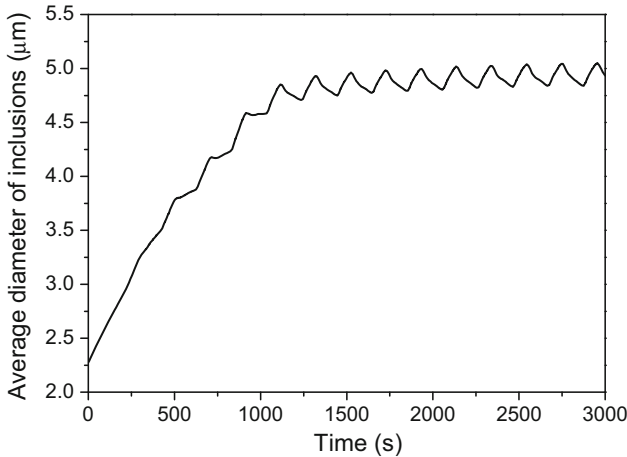


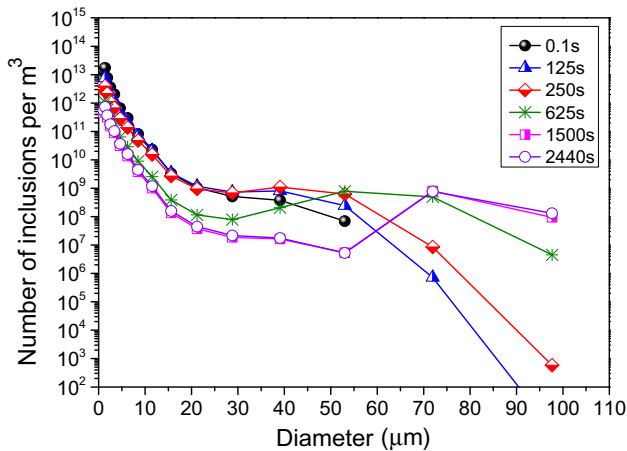Fig. 21—Variation of average diameter of inclusions in the entire tundish.



Fig. 23—Variation of number density of inclusions at different times at tundish outlet ($n_{d>100 \ \mu m} = 0$).

where $t_m$ is the mean residence time of the molten steel in the tundish (s).

It should be emphasized that the total casting time of one entire heat was 2400 seconds (40 minutes). Thus, the collision and coalescence of inclusions in the current tundish were always in an unsteady state during continuous casting. In some moments, such as from 100 to 125 seconds, there was an increase in the total volume of inclusions because the removal flux of inclusions at the top surface was zero during this period. The inclusions with large total volume flowed towards the outlet together with the molten steel, as shown in Figure 17. The inclusions with total volume of $2.15 \times 10^{-4}$ m$^3$ were near the outlet at 100 seconds, but it was $2.25 \times 10^{-4}$ m$^3$ inclusions at 125 seconds.

### D. Variation of Different Size Inclusions

In actual operations, the new incoming steel from the ladle shroud was often mixed with the remaining molten steel in the tundish. The inclusions collided with not only each other but also the new different size inclusions moving together with the molten steel from the inlet. It was a combination of multi-complicated processes. Figures 18, 19, and 20 show the concentration distribution of inclusions of three different sizes at three different moments.

The strong stirring energy in the outer area of the hole in the weir and at the bottom corner of the inlet zone in Figure 11(c) provided favorable conditions for collision and coalescence of inclusions. At the beginning (5 seconds), small-sized inclusions gradually collided with each other to form bigger size inclusions. As shown in Figure 19, the concentration of 4.61 $\mu$m inclusions in above zones was significantly larger than that in other zones and the maximum value was $1.48 \times 10^{-2}$, larger than its dimensionless initial concentration of $1.46 \times 10^{-2}$. However, there was an opposite

Table VIII.   Removal Fraction of Inclusions in the Tundish ($t = 2440$ s)

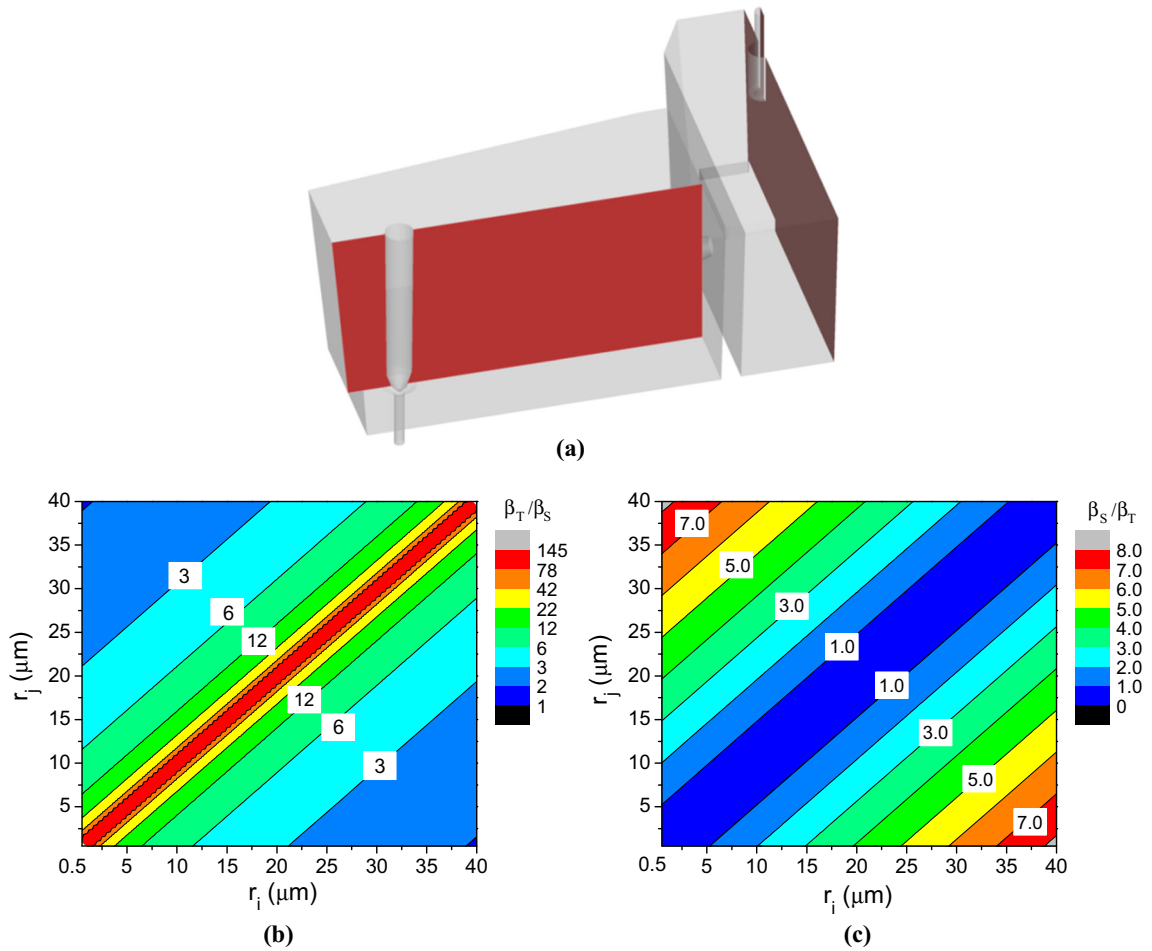| Case | Inlet (ppm) | Outlet (ppm) | Removal Fraction (pct) |
|---|---|---|---|
| Turbulent, Stokes Collision and Removal by Floating | 49.5 | 41.4 | 16.4 |

**(a)**



**(b)**



**(c)**

Fig. 24—Distribution of the ratio between $\beta_S(r_i, r_j)$ and $\beta_T(r_i, r_j)$; (b) $\beta_T(r_i, r_j)/\beta_S(r_i, r_j)$ at the symmetry plane; (c) $\beta_S(r_i, r_j)/\beta_T(r_i, r_j)$ at the red plane of the outlet region.

**Table IX.   Parameters of Al$_2$O$_3$, SiO$_2$, and 12CaO·7Al$_2$O$_3$ Inclusions in the Molten Steel**

| Inclusion | Hamaker Constant, $\times 10^{20}$ (J) | $\rho_I$ (kg/m$^3$) | $\sigma_{MS}$ (N/m) | $\mu_M$ (Pa·s) | $\theta$ (deg) |
|---|---|---|---|---|---|
| Al$_2$O$_3$ | 2.3[55] | 3990 | 1.389[68] | 0.0067 | 144[69] |
| SiO$_2$ | 3.1[55] | 2500 | 1.409[68] | 0.0067 | 115[66,70] |
| 12CaO·7Al$_2$O$_3$ | 0.85[56] | 2700[71] | 1.409[68] | 0.0067 | 54.3[69] |

concentration distribution for inclusions with 1.36 $\mu$m due to its faster dissipation rate in above zones and the minimum value was $3.62 \times 10^{-1}$ in Figure 18. In addition, the concentration of 1.36 $\mu$m inclusions in two big recirculation zones was much higher than that in other zones due to weaker turbulence. With increasing time, the generation rate of 1.36 and 4.61 $\mu$m inclusions in the entire tundish was smaller than their dissipation rate, thus resulting in a decrease in their concentrations at 75 seconds. After reaching the steady state, their concentration distribution showed a same tendency and the value in the inlet was larger than that in other zones.

Due to no sink term, the generation process played a dominant role in the change of the concentration of

97.66 $\mu$m inclusions. At 75 seconds, the maximum value was increased from $5.17 \times 10^{-18}$ to $1.13 \times 10^{-14}$. Besides, they moved towards the outlet zone together with the molten steel; thus, its concentration distribution at 2440 seconds was different from that of 1.36 and 4.61 $\mu$m inclusions. For instance, there was a maximum value of $1.03 \times 10^{-5}$ for 97.66 $\mu$m inclusions in two big recirculation zones. However, the concentrations for 1.36 and 4.61 $\mu$m inclusions in above zones were the smallest. The variation of average diameter of inclusions in the entire tundish is illustrated in Figure 21. It was interesting that the average size of inclusions firstly reached a peak value around 1110 seconds and then changed in a periodic oscillation way. As shown in

Figure 22, the average diameter of inclusions in the inlet was significantly larger than that in other zones after reaching the steady state. The maximum value was about 3.3 $\mu$m at the bottom corner of the inlet zone, and there was a minimum value of 1.1 $\mu$m in two recirculation zones. Meanwhile, the distribution of average diameter of inclusions was almost the same as the turbulent energy dissipation rate.

The change of number density of inclusions as a function of time at the outlet is plotted in Figure 23. There were no inclusions larger than 53.02 $\mu$m at the initial time and big size inclusions were gradually generated with increasing time. For instance, the number density of 71.95 $\mu$m inclusions was $7.2 \times 10^5$ #/m$^3$ at 125 seconds and it was $4.5 \times 10^6$ #/m$^3$ for inclusions with 97.66 $\mu$m at 625 seconds. The number density of the maximum group inclusions always increased because there were only the generation term and no sink term as shown in Eq. [9]. But for other groups, the number density of inclusions firstly increased and then decreased. Based on the results above, the contribution of the number density of small size inclusions to total volume or mass of inclusions gradually decreased with the collision and coalescence of inclusions proceeding, but for big size inclusions, their contribution was enhanced. Besides, the total oxygen converted from mass concentration of inclusions at the outlet at 2440 seconds is shown in Table VIII. When turbulent collision, Stokes collision, and removal by floating were included, it was 41.4 ppm and the removal fraction of inclusions was 16.4 pct.

### E. Discussion on Turbulent Collision and Stokes Collision

The average turbulent energy dissipation rate at the symmetry plane and red one of the outlet region was $3.9 \times 10^{-3}$ and $1.8 \times 10^{-5}$ m$^2$/s$^3$, respectively, and the ratio between $\beta_S(r_i, r_j)$ and $\beta_T(r_i, r_j)$ was calculated as shown in Figure 24. In most cases, the ratio between $\beta_T(r_i, r_j)$ and $\beta_S(r_i, r_j)$ was larger than 3 and the maximum value was 145 at the symmetry plane. It was clearly shown that the effect of turbulent collision on collision and coalescence of inclusions was stronger than that of Stokes collision, indicating that the turbulent collision was the most important mechanism for collision and coalescence of inclusions in the inlet. However, the Stokes collision mainly dominated the collision and coalescence of inclusions at the outlet region, as shown in Figure 24(c). According to Eq. [11], the Stokes collision was impossible for two inclusions with a same diameter. Meanwhile, there were no 71.95 and 97.66 $\mu$m inclusions at the initial time. If Stokes collision was only considered, the resulting number density of both size inclusions above was always zero. When turbulent collision was included, big size inclusions were generated and Stokes collision further promoted their generation process. Consequently, they had multiple effects on collision and coalescence of inclusions.

### F. Effect of Turbulent Fluctuation and Type of Inclusions on the Removal of Inclusions

Due to the difference in the density of inclusions, the contact angle, and interfacial tension with the molten steel, the collision time and rupture time were different for solid and liquid inclusions in the molten steel. Hence, their removal at the interface between the molten steel and slag was different. Table IX shows the parameters of Al$_2$O$_3$, SiO$_2$, and 12CaO·7Al$_2$O$_3$ inclusions in the molten steel.

Figure 25 shows variation of the total oxygen converted from mass concentration of three types of inclusions above in the tundish. In case of considering the effect of the turbulence on the inclusion removal, their total oxygen showed a fluctuation descent tendency and then reached the steady state, similar to the results in Figure 15. For 12CaO·7Al$_2$O$_3$ inclusions, the total oxygen was significantly larger than that of alumina and silica inclusions, which was caused by the smaller
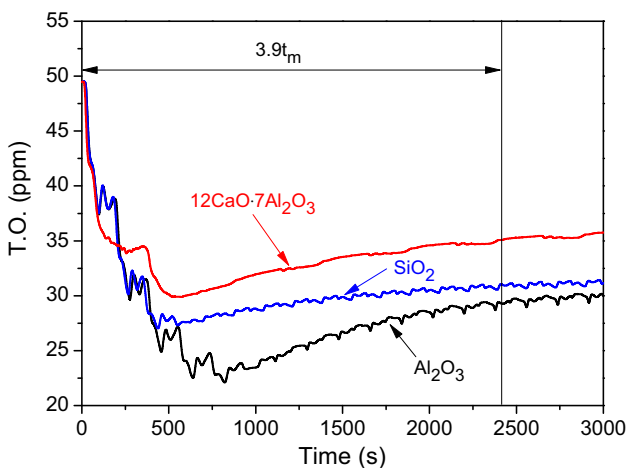


Fig. 25—Variation of total oxygen converted from mass concentration of three types of inclusions at the outlet.

**Table X. Removal Fraction of Different Type of Inclusions in the Tundish ($t$ = 2440 s)**

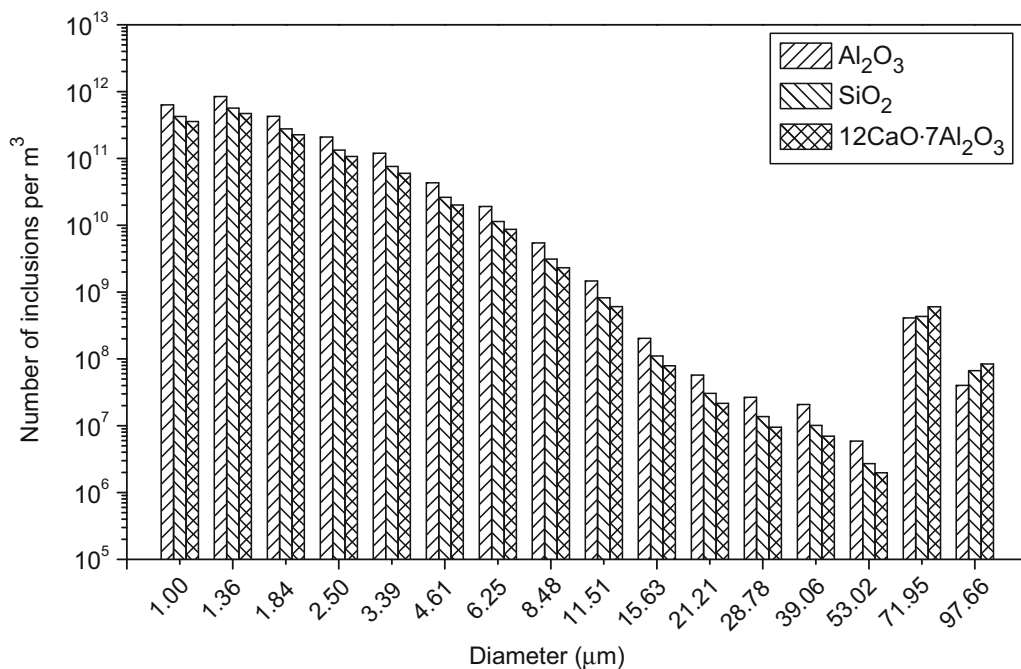| Inclusion | Inlet (ppm) | Outlet (ppm) | Removal Fraction (pct) |
| --- | --- | --- | --- |
| Al$_2$O$_3$ | 49.5 | 30.1 | 39.2 |
| SiO$_2$ | 49.5 | 31.4 | 36.5 |
| 12CaO·7Al$_2$O$_3$ | 49.5 | 36.3 | 26.6 |

Fig. 26—Variation of number density of three types of inclusions at the outlet at 2440 s.

contact angle between liquid inclusions and the molten steel. There was an inverse proportion relationship between the contact angle and the rupture time. Therefore, it was difficult for liquid inclusions with a larger rupture time to be absorbed by the slag. As shown in Table X, the removal fraction of $12CaO \cdot 7Al_2O_3$ inclusions was 26.6 pct, 12.6 pct lower than that of alumina inclusions. The small- and medium-sized inclusions gradually collided with each other to generate bigger size inclusions, so that the number density of $12CaO \cdot 7Al_2O_3$ inclusions with 71.95 and 97.66 $\mu$m was much higher than that of silica and alumina inclusions with the same diameter, as shown in Figure 26. Meanwhile, it showed an opposite tendency for other groups.

Although both of silica and alumina inclusions were solid ones, there was a big difference in the variation of their total oxygen because the silica inclusions with smaller density have a smaller contact angle with the molten steel. Their removal fractions were 36.5 and 39.2 pct, respectively. Compared with $12CaO \cdot 7Al_2O_3$ inclusions, the Hamaker constant had a big influence on the collision and coalescence of silica and alumina inclusions, which promoted the generation of the maximum group inclusions.

## VI. CONCLUSIONS

In the study, mathematical models were developed to predict the growth and removal of inclusions in the tundish. The classical removal condition of inclusions at the top slag was modified by considering the properties of inclusions and the molten steel, such as the velocity, wettability, density, size, and interfacial tension. Meanwhile, the effect of composition of inclusions on the

collision and coalescence of inclusions was considered. The conclusions are as follows.

(1) The calculated results were well validated by the measured number density of inclusions in the tundish, indicating that the current mathematical model can be used to accurately simulate the collision and coalescence of inclusions.
(2) The turbulent collision was the most important mechanism for collision and coalescence of inclusions in the pouring zone, but it was Stokes collision at the outlet region in the current tundish.
(3) The equilibrium time when the collision and coalescence of inclusions reached the steady state was 2440 seconds and was equal to 3.9 times of the mean residence time, indicating that the collision and coalescence of inclusions in the tundish were always in an unsteady state during continuous casting.
(4) The contribution of the number density of small-sized inclusions to total volume or mass of inclusions gradually decreased with the collision and coalescence of inclusions proceeding, but for big size inclusions, their contribution was enhanced.
(5) In case of considering Stokes collision, turbulent collision and removal by floating, the removal fraction of inclusions was 16.4 pct.
(6) Compared with $12CaO \cdot 7Al_2O_3$ inclusions, the silica and alumina inclusions were much easier to be removed from the molten steel and their removal fraction was 36.5 and 39.2 pct, respectively.

The adhesion of inclusions to walls, including the long, short, bottom, and internal weir should be considered in the further investigation. At the same time, the generation of inclusions begins with the nucleation and then collision, growth, and removal

exists. In future, the nucleation process is included to study the collision and coalescence of inclusions.

## ACKNOWLEDGMENTS

## REFERENCES

1. L. Zhang and B.G. Thomas: *ISIJ Int.*, 2003, vol. 43, pp. 271–91.
2. H. Gao: *Steelmaking*, 2000, vol. 16, pp. 38–43.
3. M. Goransson, F. Reinholdsson, and K. Willman: *Iron Steelmak.*, 1999, vol. 26, pp. 53–58.
4. K. Ogawa: *Nishiyama Memorial Seminar*, ISS, Tokyo, 1992, vol. 143, pp. 137–66.
5. K.W. Lange: *Int. Mater. Rev.*, 1988, vol. 33, pp. 53–89.
6. J.H. Park and H. Todoroki: *ISIJ Int.*, 2010, vol. 50, pp. 1333–46.
7. M.A. Van Ende, M. Guo, E. Zinngrebe, B. Blanpain, and I.H. Jung: *ISIJ Int.*, 2013, vol. 53, pp. 1974–82.
8. P.G. Saffman and J.S. Turner: *J. Fluid Mech.*, 1956, vol. 1, pp. 16–30.
9. K. Nakanishi and J. Szekely: *Trans. Iron Steel Inst. Jpn.*, 1975, vol. 15, pp. 522–30.
10. K. Higashitani, K. Yamaguchi, Y. Matsuno, and G. Hosokawa: *J. Chem. Eng. Jpn.*, 1983, vol. 16, pp. 299–304.
11. H. Tozawa, Y. Kato, K. Sorimachi, and T. Nakanishi: *ISIJ Int.*, 1999, vol. 39, pp. 426–34.
12. T. Nakaoka, S. Taniguchi, K. Matsumoto, and S.T. Johansen: *ISIJ Int.*, 2001, vol. 41, pp. 1103–11.
13. L. Zhang and B.G. Thomas: *7th European Electric Steelmaking Conference, Venice, Italy*, Associazione Italiana di Metallurgia, Milano, 2002, vol. 2, pp. 77–86.
14. L. Zhang, S. Taniguchi, and K. Cai: *Metall. Mater. Trans. B*, 2000, vol. 31B, pp. 253–66.
15. L. Zhang and W. Pluschkell: *Ironmak. Steelmak.*, 2003, vol. 30, pp. 106–10.
16. L. Zhang, W. Pluschkell, and B.G. Thomas: *Steelmaking Conference Proceedings.* 2002, vol. 85, pp. 463–76.
17. W. Yang, H. Duan, L. Zhang, and Y. Ren: *JOM*, 2013, vol. 65, pp. 1173–80.
18. K. Xu and B.G. Thomas: *Metall. Mater. Trans. A*, 2012, vol. 43A, pp. 1079–96.
19. D. Geng, H. Lei, and J. He: *ISIJ Int.*, 2010, vol. 50, pp. 1597–1605.
20. D. Sheng, M. Söder, P. Jönsson, and L. Jonsson: *Scand. J. Metall.*, 2002, vol. 31, pp. 134–47.
21. H. Lei, K. Nakajima, and J. He: *ISIJ Int.*, 2010, vol. 50, pp. 1735–45.
22. L. Wang, Q. Zhang, S. Peng, and Z. Li: *ISIJ Int.*, 2005, vol. 45, pp. 331–37.
23. W. Lou and M. Zhu: *Metall. Mater. Trans. B*, 2013, vol. 44B, pp. 762–82.
24. W. Lou and M. Zhu: *ISIJ Int.*, 2014, vol. 54, pp. 9–18.
25. Y.J. Kwon, J. Zhang, and H.G. Lee: *ISIJ Int.*, 2008, vol. 48, pp. 891–900.
26. L. Zhang and S. Taniguchi: *Iron Steelmak.*, 2001, vol. 28, pp. 55–78.
27. L. Zhang, S. Taniguchi, and K. Matsumoto: *Ironmak. Steelmak.*, 2002, vol. 29, pp. 326–36.
28. A.K. Sinha and Y. Sahai: *ISIJ Int.*, 1993, vol. 33, pp. 556–66.
29. H. Lei, D. Geng, and J. He: *ISIJ Int.*, 2009, vol. 49, pp. 1575–82.
30. Y. Miki, Y. Shimada, B. G. Thomas, A. Denissov. *Steelmaking Conference Proceedings.*, Iron and Steel Society of AIME, 1997, vol. 80, pp. 37-46.
31. V.D. Felice, I.L.A. Daoud, B. Dussoubs, A. Jardy, and J.P. Bellot: *ISIJ Int.*, 2012, vol. 52, pp. 1273–80.
32. J.P. Bellot, V.D. Felice, B. Dussoubs, A. Jardy, and S. Hans: *Metall. Mater. Trans. B*, 2013, vol. 45B, pp. 13–21.
33. L. Zhang: *Iron Steel Technol.*, 2010, vol. 7, pp. 55–69.
34. L. Zhang, J. Zhi, J. Mou, and J. Cui: *J. Iron. Steel Res. Int.*, 2005, vol. 12, pp. 20–27.
35. S. Taniguchi and A. Kikuchi: *Tetsu-to-Hagané*, 1992, vol. 78, pp. 527–35.
36. U. Lindborg and K. Torssell: *Trans. Metall. Soc. AIME*, 1968, vol. 242, pp. 94–102.
37. L. Zhang and S. Taniguchi: *Int. Mater. Rev.*, 2000, vol. 45, pp. 59–82.
38. Y. Ye and J.D. Miller: *Int. J. Miner. Process.*, 1989, vol. 25, pp. 199–219.
39. H.J. Schulze: *Miner. Process Extr. Metall. Rev.*, 1989, vol. 5, pp. 43–76.
40. H.J. Schulze and J.O. Birzer: *Colloids Surf.*, 1987, vol. 24, pp. 209–24.
41. Ansys Fluent 14.0. ANSYS, Inc, Canonsburg, PA, 2011.
42. V. Singh, S. Lekakh, and K. Peaslee: *62nd SFSA Technical and Operating Conference*, 2008.
43. F. Schamber: *Introduction to Automated Particle Analysis by Focused Electron Beam*, Corporation, 2009.
44. L. Zhang, B. Rietow, B.G. Thomas, and K. Eakin: *ISIJ Int.*, 2006, vol. 46, pp. 670–79.
45. S. Linder: *Scand. J. Metall.*, 1974, vol. 3, pp. 137–50.
46. O.J. Ilegbusi and J. Szekely: *ISIJ Int.*, 1989, vol. 29, pp. 1031–39.
47. Y. Miki and B.G. Thomas: *Metall. Mater. Trans. B*, 1999, vol. 30B, pp. 639–54.
48. J. Zhang and H.G. Lee: *ISIJ Int.*, 2004, vol. 44, pp. 1629–38.
49. H. Lei and J. He: *J. Non Cryst. Solids*, 2006, vol. 352, pp. 3772–80.
50. H. Lei and J. He: *Acta Metall. Sin.*, 2007, vol. 43, pp. 1195–1200.
51. S. Chakraborty and Y. Sahai: *The Sixth International Iron and Steel Congress*, Nagoya, Japan, 1990, vol. 3, pp. 189–96.
52. V. Panjkovic and J. Truelove: *Second International Conference on CFD in the Minerals and Process Industries*, CSIRO, Melbourne, Australia, 1999, pp. 399–404.
53. D.B. Hough and L.R. White: *Adv. Colloid Interface Sci.*, 1980, vol. 14, pp. 3–41.
54. R.G. Horn, D.R. Clarke, and M.T. Clarkson: *J. Mater. Res.*, 1988, vol. 3, pp. 413–16.
55. S. Taniguchi, A. Kikuchi, T. Ise, and N. Shoji: *ISIJ Int.*, 1996, vol. 36 (Suppl), pp. S117–20.
56. L. Bergström: *Adv. Colloid Interface Sci.*, 1997, vol. 70, pp. 125–69.
57. J.M. Fernández-Varea and R. Garcia-Molina: *J. Colloid Interface Sci.*, 2000, vol. 231, pp. 394–97.
58. Y.K. Leong and B.C. Ong: *Powder Technol.*, 2003, vol. 134, pp. 249–54.
59. V. Runkana, P. Somasundaran, and P.C. Kapur: *J. Colloid Interface Sci.*, 2004, vol. 270, pp. 347–58.
60. O. Bonnefoy, F. Gruy, and J.M. Herri: *Fluid Phase Equilibr.*, 2005, vol. 231, pp. 176–87.
61. L. Farmakis, N. Lioris, A. Koliadima, and G. Karaiskakis: *J. Chromatogr. A*, 2006, vol. 1137, pp. 231–42.
62. Y. Zhang, Y. Chen, P. Westerhoff, K. Hristovski, and J.C. Crittenden: *Water Res.*, 2008, vol. 42, pp. 2204–12.
63. K.Y. Liu, J.Y. Rau, and M.Y. Wey: *J. Hazard Mater.*, 2009, vol. 171, pp. 102–10.
64. B. Faure, G. Salazar-Alvarez, and L. Bergström: *Langmuir*, 2011, vol. 27, pp. 8659–64.
65. T. Mizoguchi, Y. Ueshima, M. Sugiyama, and K. Mizukami: *ISIJ Int.*, 2013, vol. 53, pp. 639–47.
66. K. Nakajima: *Tetsu-to-Hagané*, 1994, vol. 80, pp. 383–88.
67. G. Parry and O. Ostrovski: *ISIJ Int.*, 2009, vol. 49, pp. 788–95.
68. D. Bouris and G. Bergeles: *Metall. Mater. Trans. B*, 1998, vol. 29B, pp. 641–49.
69. L. Sun: University of Science and Technology Beijing, Beijing, 2013.
70. J. Wang: *J. Anshan Inst. Iron Steel Technol.*, 1986, vol. 1, pp. 23–9.
71. H. Sun, H. Yu, B. Wang, M. Yu, G. Tu, and S. Bi: *Chin. J. Nonferrous Met.*, 2008, vol. 18, pp. 1920–25.